Biomechanics of Infarcted Left Ventricle-A Review of Modelling

Wenguang Li

School of Engineering, University of Glasgow, Glasgow, UK, G12 8QQ

Wenguang.Li@glasgow.ac.uk

Date：16 June 2020

Abstract

Mathematical modelling in biomechanics of infarcted left ventricle (LV) serves as an indispensable tool for remodelling mechanism exploration, LV biomechanical property estimation and therapy assessment after myocardial infarction (MI). However, a review of mathematical modelling after MI has not been seen in the literature so far. In the paper, a systematic review of mathematical models in biomechanics of infarcted LV was established. The models include comprehensive cardiovascular system model, essential LV pressure-volume and stress-stretch models, constitutive laws for passive myocardium and scars, tension models for active myocardium, collagen fibre orientation optimization models, fibroblast and collagen fibre growth/degradation models and integrated growth-electro-mechanical model after MI. The primary idea, unique characteristics and key equations of each model were identified and extracted. Discussions on the models were provided and followed research issues on them were addressed. Considerable improvements in the cardiovascular system model, LV aneurysm model, coupled agent-based models and integrated electro-mechanical-growth LV model are encouraged. Substantial attention should be paid to new constitutive laws with respect to stress-stretch curve and strain energy function for infarcted passive myocardium, collagen fibre orientation optimization in scar, cardiac rupture and tissue damage and viscoelastic effect post-MI in the future.

Keywords: left ventricle; myocardial infarction; cardiovascular system; biomechanical model; collagen fibre; myocardium

Abbreviations

2D	two-dimensional
3D	three-dimensional
CFD	computational fluid dynamics
d	day
DPVR	diastolic pressure-volume relation
ED	end-diastolic or end of diastole
EDP	end-diastolic pressure
ECM	extracellular matrix
ES	end-systolic or end of systole
ESP	end-systolic pressure

ESPVR	end-diastolic pressure-volume relations
FE	finite element
FEA	finite element analysis
FEM	finite element model
LGE	late gadolinium enhancement
LV	left ventricle
LVEDP	Left ventricle end-diastolic pressure
LVESV	left ventricular systolic volume
MI	Myocardial infarction
MMPs	matrix metalloproteinases
MRI	magnetic resonance imaging
ODE	ordinary differential equation
PIM	percent inactive myocardium
PSM	percent shorting of myocardium
p-V	pressure-volume
RV	right ventricle
SAVER	surgical anterior ventricular restoration
TGF-β	transforming growing factor β
STE	speckle-tracking echocardiography
TIMPs	metalloproteinases
wk	week

1 Introduction

Myocardial infarction (MI) refers to death of the myocytes in a region of myocardium in left ventricle (LV) owing to the lack of oxygen caused by obstruction of the blood supply from left circumflex (LCX) and left anterior descending (LAD) arteries or their branches with stenosis, see Fig. 1. After the death of myocytes in LV, the LV loses contracting ability in part and its pump function is impaired, even heart failure emerges. According to a WHO statement, 17.4 million MI patients exist in the world every year compared with 15 million stroke patients. In the UK prevalence of coronary heart disease is 4.5% in the North East of England, and 4.3% in Scotland. The annual death rate of survivors of MI patients is 5% and six times that of people at the same age who are without coronary heart disease [1]. Around £6.8 billion was spent on the disease in the NHS of England during 2012-2013 [2].

Biomechanics of infarcted LV has become a study subject since 1960's and includes experimental and mathematical modelling contents broadly. It is the study of the structure, function, kinematics and kinetics of infarcted LVs at the organ, tissue and cell levels by employing experimental and mathematical modelling methods in mechanics.

Recently, mathematical modelling has been become indispensable and increasingly important method in biomechanics of infarcted LV in terms of great advancement in both computer and software [3]. In comparison with experimental biomechanics of infarcted LV, mathematical model-based biomechanics possesses a few essential and significant advantages, such as dealing with cases and conditions unachievable by experiment, carrying out simulations with different time scales, altering model parameters easily, very cheap in operating cost, and assessing a therapy proposal safely prior to an actual surgery taking place.

Image-based or patient-specific or personalized LV biomechanics was perfectly elucidated in [4-6]. Biomechanics of cardiac function of normal and diseased LVs was comprehensively and briefly introduced in [7]. Contemporary biomechanical models of myocardium were interpreted clearly in [8] in terms of healthy LVs. Computational modelling at cardiac cell level has been reviewed elegantly and rigorously in [9] for cardiac signalling networks and [10] for cardiac fibroblasts and fibrosis with emphasis on agent-based modelling of infarct healing as well as [11] for patient-specific LV and biomaterial inject therapy of LV post-MI. There hasn't been a comprehensive survey of mathematical modelling in biomechanics of infarcted LV in remodelling process with emphasis on variation of LV biomechanical property, myocardial remodelling and MI scar growth after MI in the literature so far [3,5,11].

In this contribution, mathematical models and their modelling methods in biomechanics of infarcted LV were summarized thoroughly in terms of a biomechanics worker point of view to provide a supplement for existing reviews and offer an opportunity for researchers to develop new ideas in mathematical modelling of remodelling post-MI in the future. The fundamental concept, experimental

evidence and LV remodelling process after MI are referred to [12] where experiments in biomechanics of infarcted LV have been reviewed.

The existing biomechanics models for remodelling after MI published since 1950's were sorted out and divided into four groups, i.e. cardiovascular system models, biomechanical models, LV aneurysm models and growth models post-MI. These models and their contributors as well as features are summarised in Table 1.

In Section 2, the cardiovascular system model and LV biomechanical models after MI are summarised. In Section 3 and 4, aneurysm models are demonstrated. In Section 5, growth models in the remodelling process post-MI are detailed. In Section 6, discussions on the models reviewed are put forward, and a few new study issues are raised. Then a conclusion is followed. Perhaps this is a comprehensive review of mathematical modelling in biomechanics of infarcted LV for the first time, especially the problem in use of LV wall curvature-based regional stress model was identified, see Section 3.10 for detail.

2 Lumped-parameter cardiovascular system model

After MI occurs, the diastolic pressure-volume relationship, LV chamber stiffness and mass should vary with time [13]. If these effects can be modelled with simple mathematical models, the results will supply some insight into the remodelling process and also are meaningful to remodelling invention and therapy.

A lumped-parameter model of the ovine cardiovascular system was developed in [14] based on the previous work [15] to clarify effects of MI size and compliance on cardiovascular function by involving a time varying elastane of LV $E_{\mathrm{LV}}(t)$ (=$1/C_{\mathrm{LV}}(t)$) proposed initially by [16] and an adaptive compensatory mechanism to maintain LV stroke volume. A diagram for the lumped-parameter model is illustrated in Fig.2. In the figure, venous, pulmonary and arterial systems are represented by a fixed flow resistance and compliance, respectively; while tricuspid, pulmonary, mitral and aortic valves are simplified to a fixed flow resistance and unidirectional diode. The right ventricle (RV) and LV are considered as a chamber with variable active compliance and passive compliance.

It is assumed that MI occurs in LV only. In remote zone, both active and passive compliances are available, and the time varying elastane in MI region is written as during systolic and diastolic phases [14]

$$\begin{cases} E_{\mathrm{LVr}}(t) = (1-V_{\mathrm{cf}})K_{LV}\, sin\frac{\pi t}{2t_p} + \frac{1}{(1-V_{\mathrm{cf}})C_{\mathrm{LVp}}}, t \in [0, t_p] \\ E_{\mathrm{LVr}}(t) = (1-V_{\mathrm{cf}})\left(\frac{1}{2K_{LV}}\right)\left(1-cos\frac{\pi t}{2t_s}\right) + \frac{1}{(1-V_{\mathrm{cf}})C_{\mathrm{LVp}}}, t \in t_p, t_s \\ E_{\mathrm{LVr}}(t) = \frac{1}{(1-V_{\mathrm{cf}})C_{\mathrm{LVp}}}, t > t_s \end{cases} \quad (1)$$

where K_{LV} is LV contractility, $V_{\mathrm{cf}}$is the MI volume fraction in LV wall, t_p is the time to peak LV contraction, t_s is the systolic phase time length, C_{LVp} is passive compliance. The first term in the first

and second expressions of Eq. (1) are relative to the active compliance C_{LVa}, and the two compliances are connected in parallel in the model, i.e. $1/C_{\mathrm{LV}}(t) = 1/C_{\mathrm{LV}a}(t) + 1/C_{\mathrm{LVp}}(t)$, then the active compliance C_{LVa} reads as

$$\begin{cases} C_{\mathrm{LVa}}(t) = \frac{1}{(1-V_{\mathrm{cf}})K_{LV}\, sin\frac{\pi t}{2T_p}}, t \in [0, t_p] \\ C_{\mathrm{LVa}}(t) = \frac{1}{(1-V_{\mathrm{cf}})\left(\frac{1}{2K_{LV}}\right)\left(1-cos\frac{\pi t}{2t_s}\right)}, t \in t_p, t_s \\ C_{\mathrm{LVa}}(t) = 0, t > t_s \end{cases} \tag{2}$$

In MI region, the compliance is always the fixed passive compliance, C_{LVf}, and the corresponding fixed elastane at any time is

$$E_{\mathrm{LVf}} = \frac{1}{C_{\mathrm{LVf}}} \tag{3}$$

Once again, the compliance in the remote zone and the compliance in MI region contribute to the total LV compliance in parallel; and the differential equation of LV pumping model is expressed by [14]

$$\frac{dp_{\mathrm{LV}}}{dt} = [E_{\mathrm{LVr}}(t) + E_{\mathrm{LVf}}]Q_{\mathrm{LV}} - p_{\mathrm{LV}}[E_{\mathrm{LVr}}(t) + E_{\mathrm{LVf}}]\frac{d\left[\frac{1}{E_{\mathrm{LVr}}(t)+E_{\mathrm{LVf}}}\right]}{dt} \tag{4}$$

The MI size and stiffness have been involved in the model Eq. (4).

Additionally, the compensatory characteristic of the cardiovascular system was considered based on the difference of between desired and actual stroke volumes and passive LV compliance with linear model [14], that is

$$\begin{cases} \Delta V_{total} = V_{total}\left(\frac{SV_d - SV}{SV_d}\right) \\ p_{\mathrm{LV}} = (V_{\mathrm{LV}} + \Delta V_{total})\left(\frac{1}{C_{\mathrm{LVp}}} + \frac{1}{C_{\mathrm{LVf}}}\right) \end{cases} \tag{5}$$

where ΔV_{total} is the total blood in the system, SV is the current LV stroke volume and SV_d is the desired stroke volume after compensation. The effects of MI size, infarct compliance and compensation on cardiac pumping function were investigated theoretically with above models.

Note that just a set of model parameters from animal model was used and not validated with clinical data [14]. Therefore, these models are subject to be improved in the future.

3 LV biomechanical models post-MI

3.1 Empirical models for LV diastolic *p*-*V* curve

LV passive pressure(*p*)-volume(*V*) curves during diastole have been measured in vitro by employing animal models since 1960's [17-20] and have been reviewed in [21]. For the first time, an empirical relationship of LV chamber pressure in terms of an exponential function of LV chamber volume is proposed in [22] to best fit in vitro experimental *p*-*V* data

$$p = b(e^{aV} - e^{aV_0}) \tag{6}$$

where a, b and c are positive constants determined by the experimental data. When $p = 0$mmHg, the LV chamber volume is in its dead volume $V = V_0$. The instant slope of a *p*-*V* curve is

$$\frac{dp}{dV} = ap + abe^{aV_0} \tag{7}$$

The equation proves that dp/dV is related to p linearly. In [23], the *p*-*V* curve and its instant slope were investigated, particularly, a dimensionless volume, i.e. $(V - V_0)/V_0 = (V/V_0 - 1)$, was used, and Eqs. (6) and (7) become

$$p = b\left[e^{a\left(\frac{V}{V_0}-1\right)} - 1\right] \tag{8}$$

and

$$\frac{dp}{d\left(\frac{V}{V_0}-1\right)} = ap + ab \tag{9}$$

It was shown that Eq. (8) could best fit the *p*-*V* curves under various conditions such as post clamp, longitudinal clamp, cross clamp and rigor mortis [20].

Since *p*-V curves reflect LV diastolic function globally without need to know LV wall passive properties in advance and can be changed by various LV diseases, they have long been applied extensively in LV disease diagnosis and assessment [22-26]. LV *p*-*V* curve and its compliance after MI were clarified by using Eqs. (6) and (7) in [27-29]. It turned out that LV with MI was subject to a large constant a compared with normal LV and LV with coronary disease [29].

3.2 Effect of MI on *p*-*V* curves

A nonlinear isotropic, initially spherical membrane model was proposed to predict LV function of an infarcted canine LV in [30]. Two-parameter strain energy density function in [31] was used to stand for nonlinear hyperelastic myocardium mechanical property in both diastole and systole. Based on a spherical model, the LV pressure can be expressed by stretch in the myocardium wall and two material property constants. These constants can be altered to reflect the difference in MI zone and remote area as well as the passive and active states.

The MI zone was considered an axis-symmetrical membrane and solved numerically by using finite difference method. Effects of infarct size and stiffness on cardiac function were investigated at various MI ages.

There is a critical issue in the model in [30]. The LV chamber pressures during diastolic and end-systolic phases were estimated by a spherical membrane model with various material parameters related to MI size, then the stresses and strains were determined with a non-spherical membrane model by applying these pressures. Obviously, the compliance from the spherical model should differ from that based on the non-spherical model under the same LV chamber pressure load. To achieve the same compliance, the material property constants in the non-spherical model need to be decided inversely according to the *p*-*V* curve given by the spherical model in the two phases.

3.3 Effects of MI on end-systolic *p*-*V* relation

Cardiac stroke volume is decided by diastolic pressure-volume relations (DPVR) and end-systolic pressure-volume relations (ESPVR) and end-diastolic pressure (EDP) and end-systolic pressure (ESP). Experimental data suggested that MI can alter ESPVR based on dog [32-35], pig and rat [36], and human models [37,38], a typical ESPVR of a dog measured in [32] is illustrated in Fig.3. Modelling altered ESPVRs by MI is complicated because myocardial contractility is involved in ESPVRs. A simple model was proposed in [32] to estimate ESPVRs in terms of MI volume fraction, stiffness of linear ESPVRs measured in normal LVs and LVs with MI.

Referring to Fig.3, the ESPVRs exhibit the nonlinear property at a low EDP, and once the pressure over a critical pressure, the relationships can be approximated to a linear function. In that case, ESPVRs were simplified to a linear relation with two parameters, namely stiffness and interception with zero pressure axis [32]. Additionally, the border zone between MI region and remote was ignored, the remote and MI zones were imaged to be two chambers sharing the same EDP and p_{es}.but different end-systolic volumes (EDV), V_{esR} and V_{esMI}. For two chambers and the original intact LV with MI, there are the following linear equations and the constraint equations for their interceptions and chamber volumes

$$\begin{cases} p_{es} = \frac{E_{esR}}{1-V_{cf}}\left[V_{esR} - (1-V_{cf})V_{0R}\right] \\ p_{es} = \frac{E_{esMI}}{V_{cf}}\left(V_{esMI} - V_{cf}V_{0MI}\right) \\ p_{es} = E_{esRMI}(V_{esRMI} - V_{0RMI}) \\ V_{esRMI} = V_{esR} + V_{esMI} \\ V_{0RMI} = (1-V_{cf})V_{0R} + V_{cf}V_{0MI} \end{cases} \tag{10}$$

where $E_{esR}/(1-V_{cf})$ is the stiffness of p_{es}-V_{esR} curve of the remote zone, E_{esR} is the stiffness of p_{es}-V_{esR} curve of the normal LV, V_{0R} is the intercept of the curve with p_{es}=0 axis, E_{esRMI} is the stiffness of p_{es}-V_{esRMI} curve of the LV with MI, V_{0RMI} is the intercept of the curve with p_{es}=0 axis as well.

Usually, E_{esR} and V_{0R} are known for a normal LV; E_{esRMI} and V_{0RMI} can be measured based on the LV with MI. The following expressions can be deduced from Eq. (10) to estimate V_{cf} or V_{0RMI} and E_{esMI}, i.e.

$$\begin{cases} \frac{1-V_{cf}}{E_{esR}} + \frac{V_{cf}}{E_{esMI}} = \frac{1}{E_{esRMI}} \\ V_{cf} = \frac{V_{0RMI}-V_{0R}}{V_{0R}-V_{0MI}} \end{cases} \tag{11}$$

If V_{cf} is known in advance, then E_{esMI} and V_{0MI} can be determined from Eq. (11). After they are available, E_{esRMI} and V_{0RMI} of the p_{es}-V_{esRMI} curve at another V_{cf} will be obtained. Based on Eq. (11), the effects of MI size on p_{es}-V_{esRMI} relationships can be decided analytically. Commonly, $E_{esMI} \gg E_{esR}$ is satisfied, thus it yields $E_{esMI} \gg E_{esR} > E_{esRMI}$.

Even though the linear ESPVR model above is simple to clinical applications, the linearity in ESPVRs is not represented [39,40] and the model may not be accurate enough. To remove this limitation in the model, Bogen et al established a biomechanical model to investigate effects of MI size on ESPVRs [41] based on an inhomogeneous LV with an infarcted axisymmetric region as used in [30] and the power-law isotropic strain energy function of Ogden type proposed in [31] and described as follows for passive LV wall

$$\psi = \frac{\mu_p}{k_p}\left(\lambda_1^{k_p} + \lambda_2^{k_p} + \lambda_3^{k_p}\right) \tag{12}$$

where λ_1 and λ_2 are in-plane principal stretches, but λ_3 is the transmural principal stretch of LV wall; μ_p and k_p are positive elastic constants of the LV wall. The corresponding in-plane Cauchy stress-stretch relationship is expressed with [41]

$$\sigma_i^p = \mu_p\left(\lambda_i^{k_p} - \lambda_3^{k_p}\right), i = 1,2 \tag{13}$$

In the active state of LV wall, the elastic constant is k_p=2 and μ_p is replaced with a constant μ_s relating to myocardial contractility. Then the active Cauchy stress developed is written as [41]

$$\sigma_i^a = \mu_s[(\lambda_i\lambda_c)^2 - \lambda_3^2\lambda_c^{-4}], i = 1,2 \tag{14}$$

where λ_c is the ratio of the diastolic rest length to the systolic rest length, λ_c=1.18 [41], λ_i is the ratio of the instant diastolic length to the diastolic rest length, as illustrated in Fig. 4. For MI zone, the total stress in LV wall is the passive Cauchy stress only. However, the total Cauchy stress is the sum of two parts σ_i^a and σ_i^p in remote zone, i.e.

$$\sigma_i = \mu_s[(\lambda_i\lambda_c)^2 - \lambda_3^2\lambda_c^{-4}] + \mu_p\left(\lambda_i^{k_p} - \lambda_3^{k_p}\right), i = 1,2 \tag{15}$$

Eq. (13) and (15) make the constitutive laws for the remote and MI regions, respectively, and have been involved in finite element analysis (FEA) in [41] based on nonlinear membrane mechanical model.

The computational input data of the model can be found in [41]. For the normal LV, μ_s=250mmHg (inotropy), two constants μ_p=2mmHg and k_p=16 are imposed. For the acute infarcted LVs with infarct sizes of 15%, 25% and 41%, respectively, constants μ_p=7.9mmHg and k_p=13 for the MI zone, but μ_p=2mmHg and k_p=16 remain for the remote zone under two conditions: normal inotropy μ_s=250mmHg and 20% increased inotropy μ_s=300mmHg in the remote zone. EDP=12mmHg was held for all infarcted LVs. The normalized EDV and ESV were made with the early diastolic LV volume. The estimated ESPVRs are demonstrated in Fig.5. Rightward shifting ESPVRs along with decreased slope in comparison with the normal LV are observed, suggesting a declined stroke. The increased contractility/inotropy in the remote zone after MI can slightly mitigate the shifting only. The limitations in the model have been addressed completely in [41].

3.4 Effects of MI on ejection fraction

A nonlinear constitutive law for passive myocardium and an empirical tension formula for active myofibers were developed in [42] and applied to simulate systolic isovolumic contraction and ejection phases respectively in [43] for identifying effects of MI size on ejection fraction (EF). The constitutive law and the formula are presented as follows

$$\begin{cases} \sigma = \frac{c}{k}[exp(k\varepsilon) - 1] \\ T_a = \alpha(t)A \end{cases} \tag{16}$$

where c and k are material constants for passive myocardium and determined with existing uniaxial tensile test results, T_a is time-varying active tension devolved in myofibre which is considered a truss element in FEA model, A is the cross-element area of the truss element, $\alpha(t)$ is a time-varying activation factor, which varies in a cardiac cycle and is identical for all myofibres. The activation factor is taken as an independent input variable and its value is decided by matching the predicted LV p-V loop to the in vivo measurement. In MI zone, $\alpha(t)$ is reduced but c and k remain unchanged in comparison with remote zone. It was shown that an increasing MI size can lead to linearly declined EF [43].

3.5 Empirical models for stress-strain curve

For ribbit mesentery uniaxial tested specimens, when scattered $d\sigma/d\lambda$ points are plotted in terms of stress σ, they can be best fitted by using a quadratic expression shown in Fig.6a. However, the coefficient of the 2nd-order term is very small, as such, the quadratic term can be removed without introducing a noticed error, and the curve fitting equation is written as [44]

$$\frac{d\sigma}{d\lambda} = a(\sigma + b) \tag{17}$$

This stress expression is empirical and has been significantly used to correlate tension-stretch or stress-stretch or stress-strain relationships in uniaxial elongation of soft biological tissue. Note that Eq. (7) and Eq. (17) share the identical form of expression. The other types of uniaxial stress-stretch relationships reviewed should be referred to [21].

Mathematical model Eq. (17) was applied to extract passive elasticity of myocardium tissue after MI to quantify mechanical dysfunction of the tissue in rabbits in [45], and the curve fitted is shown by the straight line in Fig.6b based on the first 15 data points at low loads only. In fact, the curve fitted should be the dashed line in the figure based on more data points. This problem seems to be overlooked in [45].

Even though passive myocardium is in nonlinear behaviour, it is still considered to be linear with three constant Young's moduli of 8, 16, 16kPa, rigidity moduli of 5.41, 5.41, 5.41 kPa and Poisson ratios of 0.24, 0.48, 0.48, respectively, in the longitudinal, circumferential and cross wall directions in 3D LV FEA model from biplane cine-angio-cardiographs during diastole in [46]. The Young's modulus of MI region is the value of Young's modulus of collagen fibre in the range of (200-1150)kPa. Lower

infarct and anterior infarct were involved in the FEA model, and the upper and anterior infarcts affect the whole LV movement, but the lower infarct just alters the apex movement.

Regional segmental motion after MI in seven dog LVs was measured by using ultrasonic crystals implanted in LV wall during the withdrawal of 500ml of blood and the transfusion of 800ml of blood, and the tension in LV wall was estimated by using the Laplace's law for a spherical membrane model [47]. The relationship between tension and length of LV segment is developed such as

$$T = \exp\left[10 \times a \times \left(\frac{L}{L_0}\right) + b\right] \tag{18}$$

where T is tension in LV wall, L is the instantaneous length of the MI segment and L_0 is the length at ED before MI, a and b are the parameters fitted by tension-length scattered data.

3.6 Isotropic MI scar biomechanical property

Infarct scar samples (10-15mm per side, 1-2mm thin) harvested from rat LVs wall at 3wk after MI were stretched by using a biaxial testing device [48]. For collagen fibres, there isn't a preferred orientation at 3wk, therefore, an isotropic nonlinear humongous constitutive law is proposed to fit the experimental stress-stretch data [48]

$$\psi = c(I_1 - 3)^2 \tag{19}$$

where ψ is strain energy density function, c is model constant determined from the experimental stress-stretch data, I_1 is the first invariant, I_1=tr($\mathbf{C}$), $\mathbf{C}$ is the right Cauchy-Green deformation tensor, $\mathbf{C} = \mathbf{F}^{\mathrm{T}}\mathbf{F}$, $\mathbf{F}$ is deformation gradient tensor, $\mathbf{F}^{\mathrm{T}}$ is the transpose of $\mathbf{F}$.

3.7 Estimation of passive biomechanical property constants with MI

Passive material property constants of infarcted and remote myocardia and the orientation of collagen fibres in infarcted region were determined at 1wk after MI in [49] based on MRI imaging data, catheterized blood pressure in porcine LVs in terms of Guccione and his co-worker's constitutive law for passive myocardium in [50] during diastole. The strain energy function is transverse isotropic and reads as follows [50]

$$\begin{cases} \psi = \frac{1}{2}c(e^q - 1) \\ q = b_f E_{11}^2 + b_s(E_{22}^2 + E_{33}^2 + E_{23}^2 + E_{32}^2) + b_{\mathrm{fs}}(E_{12}^2 + E_{21}^2 + E_{13}^2 + E_{31}^2) \end{cases} \tag{20}$$

where c, b_f, b_s and b_{fs} are positive constants under determination during diastole; E_{11} is the Green-Lagrange strain in the myofibre direction, E_{22} is the cross-fibre in-plane strain, E_{33} is the radial strain transverse to the fibre direction, and the rest shear strains. The model Eq. (20) was input into LS-DYNA by using a user subroutine.

A reference configuration and a current configuration of LV for FEA were generated based on MRI image at early-diastolic and end-diastolic (ED) phases, respectively. The reference configuration was loaded inside with 10mmHg measured LV pressure at ED phase to get a computed current configuration. Then its LV chamber volume and strains in seven rings were compared with those from

MRI at ED phase. Four parameters (c, b_f, b_s, b_{fs}) in remote region and four parameters (c, b_f, b_s, b_{fs}) in MI region along with myofibre angles at epicardium and endocardium were adjusted by using genetic algorithm (GA) in the software LS-OPT to minimize the following objective function

$$F = \sum_{n=1}^{N}\sum_{i=1}^{3}\sum_{j=1}^{3}\left(E_{ij,n}^{\mathrm{FEA}} - E_{ij,n}^{\mathrm{MRI}}\right)^2 + \left(\frac{V_{\mathrm{LV}}^{\mathrm{FEA}} - V_{\mathrm{LV}}^{\mathrm{MRI}}}{V_{\mathrm{LV}}^{\mathrm{MRI}}}\right)^2 \tag{21}$$

where $E_{ij,n}^{\mathrm{FEA}}$ is the computed strain in FEA, $E_{ij,n}^{\mathrm{MRI}}$ is the strain from MRI images in seven rings in end-diastolic phase; $V_{\mathrm{LV}}^{\mathrm{FEA}}$ and $V_{\mathrm{LV}}^{\mathrm{MRI}}$ are the LV chamber volumes at ED phase respectively from FEA and MRI images, N =252 is the total number of points compared in seven rings.

Infarcted myocardium was stiffer than remote myocardium and collagen fibres were orientated more circumferentially at 1wk after MI [49]. Because just ED configuration is compared, the property constants determined are unable to ensure the agreement in strains and LV volume between FEA and MRI in mid-diastole.

An updated Mooney-Rivlin strain energy constitutive model for isotropic, incompressible, homogeneous, hyperplastic materials was proposed in [51-53] to provide a constitutive model for anisotropic myocardium with MI. The constitutive law reads as

$$\psi = a_1(I_1 - 3) + b_1\left[e^{b_2(I_3-3)} - 1\right] + \frac{k_1}{2k_2}\left[e^{k_2(I_4-1)^2} - 1\right] \tag{22}$$

where the first two terms are for the matrix material, and the last term accounts for the myofibres; a_1, b_1 and b_2 are the property constants for the matrix, k_1 and k_2 are the property parameters for the myofibres.

3.8 Phenomenological active stress model with MI

A phenomenological active stress model for LV with MI was proposed based on the well-known Hill's three-element model in [54] by Bovendeerd et al in [55]. The slightly adapted Hill velocity-stress relation is written as [55]

$$\begin{cases} -\frac{1}{v_1}\frac{dl_c}{dt} = f_v\left(\frac{T_a}{T_1}\right) \\ \frac{T_a}{T_1} = f_T f_l(l_c) f_t(t, l_s)\left(\frac{l_s - l_c}{l_{se}}\right) \\ \sigma_a = \frac{T_a l_s}{l_{s0}} \end{cases} \tag{23}$$

where v_1 is the asymptote shortening velocity, v_1 =15μm/s at the asymptote stress T_1 =110kPa. $f_v(T_a/T_1)$ is a known function ofT_a/T_1, T_a and σ_a are instant Piola-Kirchhoff stress and Cauchy stress, respectively; f_T is an index indicting the contractility of myofiber, f_T=0 in MI zone, but f_T=1 in the remote zone; l_c is the instant length of contractile element, l_s is the instant sarcomere length, l_{s0} is the reference length of sarcomere; l_{se} is the maximum length of the series elastic element, l_{se} =0.05μm; $f_l(l_c)$ is a known function of l_c; $f_t(t, l_s)$ is a known function of cardiac time t at different lengths of sarcomere. $f_v(T_a/T_1)$, $f_l(l_c)$ and $f_t(t, l_s)$ have been presented as plots in [55]. Eq. (23) can be

integrated with respect to cardiac time to get the active stress along the myofibre in a cardiac cycle. The total Cauchy stress is the sum of passive stress in the myocardium and active stress along the myofibre

$$\boldsymbol{\sigma}=\boldsymbol{\sigma}_{\mathbf{p}}+\sigma_a\mathbf{e}_{\mathbf{f}}\otimes\mathbf{e}_{\mathbf{f}} \tag{24}$$

where $\mathbf{e}_{\mathbf{f}}$ is the orientation vector of myofibre.

A phenomenological active stress model of myofibre in LVs with MI was developed in [53] at end-systole (ES) based on sarcomere length. The model is applicable to the remote region and the border zone. During systole, in the remote region and the border zone the total stress is composed of passive and active stresses. The stress components in the fibre, fibre-cross-fibre and fibre-radial coordinate system are expressed in terms of the second Poila-Kirchhoff stress [56]

$$\sigma_{ij}=\frac{1}{2}\left(\frac{\partial\psi}{\partial E_{ij}}+\frac{\partial\psi}{\partial E_{ji}}\right)-wg^{ij}+\sigma_a(l)\delta_1^i\delta_1^j, i,j=1,2,3 \tag{25}$$

where ψ is the strain energy function in Eq. (20); g^{ij} is contravariant metric tensor referred to fibre coordinates, $g^{ij}=\left(\partial f^i/\partial x^k\right)\left(\partial f^j/\partial x^k\right)$, $k=1,2,3$ for the fibre, fibre-cross-fibre and fibre-radial directions; x^k are deformed Cartesian coordinates, w is the Lagrange multiplier needed to enforce material incompressible condition; δ_1^i and δ_1^j are Kronecker delta, $\sigma_a(l)$ is given by [56]

$$\sigma_a(l)=\sigma_{a\max}\frac{Ca_0^2}{Ca_0^2+Ca_{50}^2}\left\{\frac{1}{2}\left[1-\cos\left(\frac{0.25+l_t}{l_t}\right)\pi\right]\right\}, l_t=1.0489l-1.429 \tag{26}$$

where σ_{amax} is the isometric active stress at the longest sarcomere and maximum peak intracellular calcium concentration Ca_{max}; Ca_0 is constant calcium concentration, hereCa_{max}=Ca_0=4.35μmol/L; Ca_{50} is dependent on sarcomere instant length

$$Ca_{50}=\frac{Ca_{\max}}{\sqrt{e^{4.75(l-l_0)}-1}}, l=l_R\sqrt{2E_{11}+1} \tag{27}$$

where l_0 is the sarcomere length at which no active stress generates;l is the instant sarcomere length, l_R is the sarcomere length in the unloaded reference configuration, and varies linearly from 1.78μm at endocardium to 1.91μm at epicardium [56]. In model Eq. (26), the model parameter σ_{amax} needs to be determined based on LV volume and pressure at ED.

In [57], finite element (FE) models were established for infarcted sheep LVs at 8wk after injecting calcium hydroxyapatite-based tissue filler based on 3D ultrasound images at ED and ES. Passive biomechanical property constant c in the passive constitutive law Eq. (20) and the maximum active stress σ_{amax} in the active stress model Eq. (26) were determined at ED and ES inversely. It was shown that the matrix stiffness was increased markedly and the wall stress in the infarcted zone was reduced significantly after the treatment.

A FE model of a dog LV model with a large anteroapical infarct was developed in free FE software Continuity 6.3b based on MRI images at ES [58]. The myocardium passive model Eq. (20) and the active model Eq. (26) were employed. Myofibre orientation in MI zone was changed to examine

its effect on LV pumping function. Firstly, the LV was inflated to 15mmHg from zero. Secondly, it was subject to an isovolumetric contraction at ED. Finally, the LV experienced an ejection and ended up with 100mmHg ES pressure. It was identified that the MI zone with high longitudinal stiffness but low circumferential stiffness can increase EDV, leading to the best stroke volume. This result is useful for designing therapies to improve LV pumping function by alternating MI zone biomechanical property.

In [59,60], the constitutive law for passive myocardium proposed in [61], and the active stress in [62] were integrated together and implemented in a custom immersed boundary (IB)/finite element (FE) solver to estimate prognosis of MI based on patient-specific LV models generated by using MRI images at ED and ES. The passive strain energy function value of the LV wall was increased by 50times linearly from the remote to the MI zone, and the active tension is decreased from the reference tension $T_{\max}$ in the remote region to zero in the MI zone. The eight constants were determined by minimizing the difference in the strain and LV volume between MRI and IB/FE prediction at early diastole and ED, $T_{\max}$ tension was decided by the LV volume in ED and ES.

3.9 LV model with active tension and electro-mechanics after MI

In [63], the two-variable cardiac electro-mechanical model in [64], passive myocardium constitutive law in [61], generalized muscle contraction Hill's model for active myocardium in [65] were put together to form a framework to predict the cardiac cycle of an LV with MI. In the integrated model, during isovolumetric contraction and relaxation phases and filling phase, the LV pressure was modelled with Signorini's model, but during ejection phase, the pressure was determined with three-element Windkessel model. MI zone was treated as stiffer scar without electro-mechanical and contractile effects.

It is showed that a large-sized (covering 50^o azimuthal angle range) MI can make LV pumping function poor in comparison with a small-sized (30^o) MI [63].

2.10 Regional stress model after MI

A widely used formula for calculating the meridional/longitudinal stress in myocardium was proposed in [66] based on the force balance on the coronal section as presented in Fig.7a and thin-walled membrane mechanical model. The formula is written as

$$\sigma_l = \frac{pR}{2h\left(1+\frac{h}{2R}\right)} \tag{28}$$

where σ_l is meridional/longitudinal stress, R is the radius of LV chamber inner surface, h is thickness of LV wall, p is LV chamber blood pressure. This formula is just applicable to the equator of LV.

In [67], the other two expressions for estimating the circumferential mean stress in myocardium were based on thick-walled membrane mechanical model, and read as

$$\overline{\sigma}_c = p\frac{\Delta A_c}{\Delta A_w} \tag{29}$$

and

$$\begin{cases} \overline{\sigma}_c = \dfrac{prR\left(2-\frac{r}{R}\sin\phi\right)}{2h\sin\phi\left(R+\frac{h}{2}\right)} \\ \overline{\sigma}_l = \dfrac{pr^2}{2h\sin\phi\left(r+\frac{h}{2}\sin\phi\right)} \end{cases} \tag{30}$$

Since $\sin\phi = r/R$, then Eq. (30) is in the following form

$$\begin{cases} \overline{\sigma}_c = \dfrac{pR\left[2-\left(\frac{r}{R}\right)^2\right]}{2h\left(1+\frac{h}{2R}\right)} \\ \overline{\sigma}_l = \dfrac{pR}{2h\left(1+\frac{h}{2R}\right)} \end{cases} \tag{31}$$

On the equator, $r = R$, thus $\overline{\sigma}_c$=$\overline{\sigma}_l$ in Eq. (30) and two stresses are equal to σ_l in Eq. (28). Otherwise, $\overline{\sigma}_c$>$\overline{\sigma}_l$. Eq. (28) is the exact solution of thin-walled membrane mechanical model on the LV equator, while Eq. (30) is the approximate solution of thick-walled membrane mechanical model at anywhere on LV wall. $\overline{\sigma}_c$ in Eq. (29) is subject to (5-25)% errors against the stress from FEA, and $\overline{\sigma}_c$ in Eq. (31) is with (12-20)% errors, and there is no information about the error in $\overline{\sigma}_l$against the stress from FEA [67]. Since $\overline{\sigma}_c \geq \overline{\sigma}_l$ is always held, attention should be paid to $\overline{\sigma}_c$ rather than $\overline{\sigma}_l$. Unfortunately, most existing work has been devoted to $\overline{\sigma}_l$ [68-71].

In [68], Eq. (28) was applied to estimate mean LV wall stress at peak systolic pressure based on the integration of the short-axis and long axis curvatures from MRI images. However, this application seems incorrect because Eq. (28) is applicable to the LV equator only and R is just the radius of LV chamber inner surface rather than the radius of the mid-wall curvature in the long-axis image. Further, Eq. (29) was used to estimate mean stress in LV wall as well. However, the stress from this equation is circumferential and has nothing to do with that from Eq. (28).

Similar work was found in estimations of ES LV wall stress in patients with re-perfused MI based on the radius of the mid-wall curvature from MRI images [68-71]. Eqs. (28) and (29) were still in use.

Based on the Laplace's law, for thin-walled ellipsoidal membrane LVs, the circumferential and longitudinal wall stresses are calculated with the flowing equations [72]

$$\begin{cases} \sigma_c = \dfrac{pR_c}{2h}\left(2-\dfrac{R_c}{R_m}\right) \\ \sigma_l = \dfrac{pR_c}{2h} \end{cases} \tag{32}$$

where R_c is the radius of curvature normal to meridian of a LV mid-wall, R_m is the meridional radius of curvature of the mid-wall. R_c and R_m were determined by fitting meridional contours measured on the rat healthy and infarcted LVs in vitro at both ED and ES, and the corresponding two stresses were estimated with Eq. (32) [72]. It was identified that the infarcted LVs are subject to a high-level stress in comparison with the healthy LVs.

Before and after the infarcted region was removed surgically, i.e. by using surgical ventricular restoration (SVR) technique, MRI images of 40 patients were taken in [73]. The LV regional shape, in terms of curvedness, wall stress and LV systolic function were investigated based on 3D LV surface

shape mathematical descriptors developed in [74]. The pressure-normalized stress σ_{ES}/p_{ES} and ES wall stress σ_{ED} were calculated in terms of the inner radius of curvature R and local LV wall thickness h by using membrane mechanical model, such that

$$\begin{cases} \dfrac{\sigma_{ES}}{p_{\mathrm{ES}}} = \dfrac{R}{2h\left(1+\frac{h}{2R}\right)} \\ \sigma_{\mathrm{ES}} = \dfrac{p_{\mathrm{ES}}R_{\mathrm{ES}}}{2h\left(1+\frac{h}{2R_{\mathrm{ES}}}\right)} \end{cases} \tag{33}$$

where p_{ES} is the ES pressure and is estimated by using systolic arterial pressure multiplied with a factor of 0.9 [75]. It is dominated that although SVR can reduce wall stress and improve LV systolic function, regional LV shape and function don't change much. Eq. (33) is identical to Eq. (28) and was applied to the LV equator only. In fact, σ_{ES} in Eq. (33) is $\overline{\sigma}_l$ in Eq. (31).

$\overline{\sigma}_c$ in Eq. (29) has been espoused to calculate LV regional wall stress at ED and ES in dilated cardiomyopathy in 17 patients in [76]. $\overline{\sigma}_c$ in Eq. (30) has been used correctly in determining the circumferential stress in normal, ischemic/MI and re-perfused myocardium of 25 mongrel dogs [77]. Ischemia can increase LV systolic length index (SLI), which is the systolic length measured between two markers on LV surface, and then divided by the systolic length at the baseline and multiplied by 10, and stress level, and reperfusion can reduce SLI but not the stress level, as shown in Fig.8.

Recent work indicates that ES wall stress is increased after acute MI and is an independent predictor of post-discharge heart failure, but MI size and microvascular obstruction are not [78].

3.11 Modelling collagen fibre orientation in MI zone

A biomechanical method was put forward to identify the effect of collagen fibril alignment on LV function post-MI based on a four-region (three for the remote and one for the MI), multi-scale, cylindrical model of infarcted LV in [79]. The remote zone was modelled with the constitutive laws expressed with Eqs. (20) and (26). The MI zone was composed of matrix material and one filament of crimped collagen fibrils developing on the surface of a cylinder in a helical pattern. The parameters describing the geometry of the family of collagen fibrils include axial length and radius of the cylinder, and the radius and spiral angle of the filament.

The strain energy function of MI zone is composed of the neo-Hookean model ψ_m for the mechanical property of the matrix and the strain energy function ψ_{col} for individual filaments of collagen fibrils and yields the following expression

$$\begin{cases} \psi_{\mathrm{IF}} = (1-V_{\mathrm{col}})\psi_m + V_{\mathrm{col}}\psi_{\mathrm{col}} \\ \psi_m = c_m(I_1-3) \\ \psi_{\mathrm{col}} = \int_1^{\lambda_{\mathrm{col}}} P_{\mathrm{col}}\left(\lambda, K_{\mathrm{col}}, \frac{R_{\mathrm{col}}}{r_{\mathrm{col}}}, \theta_0\right) d\lambda \end{cases} \tag{34}$$

where V_{col} is the volume fraction of collagen fibrils in MI zone, V_{col}=0.4; c_m is the matrix material constant, c_m=5.72kPa; I_1 is the first invariant of the right Cauchy-Green deformation tensor; λ_{col} is the stretch along a fibril filament; P_{col} is the first Poila-Kirchhoff stress of individual collagen filament,

which is a function of stiffness of filament K_{col} (=1.16MPa), radius of filament r_{col} and radius of the cylinder R_{col} where a filament develops, $R_{\mathrm{col}}/r_{\mathrm{col}}$=2.39; θ_0 is the crimp angle of a filament, θ_0=25.5°; the expression of P_{col} can be found in [80].

The simplified four region LV structure was analysed by using thin-walled membrane mechanical mode. The model is with fixed boundary condition on top of the LV along with two constraints in stretches and shear deformation in four regions in the circumferential and longitudinal directions under a pressure load. The collagen fibre angle was changed between -90° and +90° to identify its effect on LV pumping function. It was illustrated that for maximized LV function collagen fibres should be orientated longitudinally [79].

Notice that there is no evidence showing that collagen fibres around myofibre sheet are crimped collagen fibrils currently. Thus, the collagen fibre model used in [79] doesn't sound reasonable, and the cylindrical LV model in it is also out of date.

Based on observations on microscopical structure and orientation of large collagen fibres in the porcine and canine myocardial scars after MI, a biomechanical model was established for the large collagen fibres in the scars in terms of five coefficients determined by transmural variation of collagen fibre orientation in [81]. MI scars are highly aligned in each transmural layer and mean collagen fibre angle varies in a similar manner to healthy myofibres but with a narrow variational range across the LV wall. In each transmural layer, the orientation of individual large collagen fibre is measured from the local mean fibre angle, and the material coordinate system is aligned with the mean fibre orientation, cross-fibre and radial directions. Because the large collagen fibre is perpendicular to the radial direction, the radial component of the fibre directional vector is eliminated, and the collagen fibre directional vector is expressed by [81]

$$M=\begin{bmatrix}\cos(\theta_i-\theta_{mean})\\ \sin(\theta_i-\theta_{mean})\\ 0\end{bmatrix}^T\begin{bmatrix}E_{\mathrm{ff}} & E_{\mathrm{fc}} & E_{\mathrm{fr}}\\ E_{\mathrm{cf}} & E_{\mathrm{cc}} & E_{\mathrm{cr}}\\ E_{\mathrm{rf}} & E_{\mathrm{rc}} & E_{\mathrm{rr}}\end{bmatrix}\begin{bmatrix}\cos(\theta_i-\theta_{mean})\\ \sin(\theta_i-\theta_{mean})\\ 0\end{bmatrix} \tag{35}$$

where i stands for an individual large collagen fibre, $i=1,2,\ldots,k$, and k is the total number of large collagen fibres; θ_i is fibre angle of individual large collagen fibre i;θ_{mean} is mean fibre angle of large collagen fibres; E_{ff}, E_{fc},…,E_{rr} are the Lagrange-Green strain components in the material coordinate system. It was assumed that scars are incompressible hyperelastic material with an experiential strain energy function like Eq. (20), but with two terms such as isotropic term and collagen fibre term in the exponent. The function is expressed as follows [81]

$$\begin{cases}\psi=\frac{1}{2}c(e^q-1)\\ q=b_1(I_1-3)+b_2\left[b_3E_{\mathrm{ff}}^2+b_4E_{\mathrm{cc}}^2+b_5\left(2E_{\mathrm{ff}}E_{\mathrm{cc}}+E_{\mathrm{fc}}^2+2E_{\mathrm{fc}}E_{\mathrm{cf}}+E_{\mathrm{cf}}^2\right)\right.\\ \quad\left.+b_6(2E_{\mathrm{ff}}E_{\mathrm{fc}}+2E_{\mathrm{ff}}E_{\mathrm{cf}})+b_7(2E_{\mathrm{fc}}E_{\mathrm{cc}}+2E_{\mathrm{cf}}E_{\mathrm{cc}})\right]\end{cases} \tag{36}$$

where c, b_1 and b_2 are biomechanical constants, b_3 to b_7 are the constants related to collagen fibre orientation and histological collagen area fraction measured at each transmural layer. Theses constants are written as

$$\begin{cases} b_3 = \sum_{i=1}^{k} h_i \cos^4\left(\theta_i - \theta_{mean}\right) & b_4 = \sum_{i=1}^{k} h_i \sin^4\left(\theta_i - \theta_{mean}\right) \\ b_5 = \sum_{i=1}^{k} h_i \cos^2\left(\theta_i - \theta_{mean}\right)\sin^2\left(\theta_i - \theta_{mean}\right) & b_6 = \sum_{i=1}^{k} h_i \sin\left(\theta_i - \theta_{mean}\right)\cos^3\left(\theta_i - \theta_{mean}\right) \\ b_7 = \sum_{i=1}^{k} h_i \sin^3\left(\theta_i - \theta_{mean}\right)\cos\left(\theta_i - \theta_{mean}\right) & h_i = \dfrac{F\left(\theta_i - \theta_{mean}\right)}{k} \end{cases} \quad (37)$$

where h_i is weighted histological collagen area fraction, $F\left(\theta_i - \theta_{mean}\right)$ is histological collagen area fraction.

Constants b_3 through b_7 were calculated from collagen fibre angle distributions measured transmurally in a 3wk aged porcine scar and the stresses along the fibre and cross-fibre directions were estimated with the biomechanical constants c=0.5kPa, b_1=1.0 and b_2=100 under an equal-biaxial tensile condition, showing a variable stress pattern across the scar wall, especially the stress along the fibre direction. The stress is 45 times higher than the stress along the cross-fibre direction at 50% wall depth in the scar [81].

Very recently, effects of collagen fibre pattern on MI scar biomechanical behaviour of a rat LV sample were numerically investigated in [82] based on in-plane 2D multiscale FE method, which was proposed in [83,84]. Three collagen fibre patterns, i.e. isotropic, homogeneous (all fibres with a preferred orientation), heterogenous (fibres preferred orientations depending on regions), were generated artificially. The collagen fibre was modelled with an exponential constitutive law in items of fibre Green strain [82-84]

$$F = \frac{\kappa A}{B}\left(e^{B\lambda_G} - 1\right) \quad (38)$$

where F is fibre force, κ is fibre modulus, κ=10MPa, A is fibre cross-sectional area, A=0.0314mm^2, B is model constant, B=2.5, and λ_G is fibre Green strain. The FE model size is 4mm×4mm and 0.25mm thick, the model is subject to uniform biaxial in-plane extension at its edges.

It was demonstrated that the heterogenous fibre orientation pattern can result in more reduced anisotropy and higher intensified local stress level than the homogeneous pattern. This fact suggests that such a heterogenous pattern may impair myocardial biomechanical property potentially.

4 LV aneurysm modelling post-MI

4.1 LV Aneurysms after MI

LV aneurysms are thin-walled fibrous outpouchings of LV without contractibility and mainly located at LV apex. LV aneurysms occur after transmural MI likely prompted by the use of steroids and nonsteroidal anti-inflammatory agents [85] at an incidence rate of (3.5-5)% [86]. LV aneurysms can result in congestive heart failure, thromboembolism and late heart rupture [85].

In consequence, LV aneurysm formation has been investigated from a mechanical point of view since 1940's. The tackled issues for aneurysm formation are included: (1) effect of an aneurysm on LV

function; (2) deformable multi-layer model; (3) deformable multi-layer model with isotropic nonlinear myocardium; (4) single-layer balloon model with isotropic nonlinear myocardium; (5) biomechanical properties of LV aneurysms.

4.2 Rigid aneurysm model

LV chamber volume change was studied theoretically from ED to ES by employing a rigid aneurysm model in [87]. A spherical LV with an aneurysm in circular or rectangular-square shape was assumed in ED and ES firstly. Then the LV chamber volumes were calculated under the condition where the aneurysm shape and size were fixed in both ED and ES. The percent shorting of myocardium (PSM) was clarified in terms of the percent inactive myocardium for a circular aneurysm and rectangular-square aneurysm. Based on an LV example, it was demonstrated that a rectangular-square aneurysm could induce a larger PSM than a circular did at the same PIM value.

In this rigid or fixed aneurysm model, there is a sharpen discontinuity between the remote and the MI zone at ES. This behaviour is unrealistic because aneurysms are still deformable even without contractility.

4.3 Deformable multilayer models

LV wall is composed of four-layer myofibre muscle arrangements originating the atrioventricular ring and running in a spiral manner around LV chamber [88,89]. The four-layer cross-sectional structure is present in Fig.9, including pericardial superficial bulbo-spiral muscle, deep bulbo-spiral muscle, deep sino-spiral muscle and endocardial superficial sino-spiral muscle, respectively [89].

The deep bulbo-spiral muscle forms around 60% LV wall thickness at the base and attributes to the final emptying of LV and maintains systemic blood pressure at ES. Damage to this muscle can result in a considerable fall of blood pressure and frequent sudden death. When this muscle buddle is in relaxation, the aortic valves close. The sino-spiral muscle usually forms 30% LV wall thickness at the base [90].

When MI occurs, infarcted cardiac muscle becomes powerless to contract but with a certain tensile strength firstly. Then the dead muscle is liquefied by autolysis and cellular reaction taking place with the nearby healthy tissue. At the margin of the infarct, fibroblasts and capillaries grow and spread into the MI zone and eventually replace the zone with mature collagen fibrous tissue. Further on, the collagen tissue dehydrates and leads to a dense scar of the fibre [88].

Obviously, at the MI liquefying stage, the MI is subject to the weakest mechanical strength. In a cardiac cycle, the LV chamber is under the maximum pressure loading during the isometric phase just before the aortic valves open. In these two circumstances, an aneurysm most likely arises. This problem was tackled at the MI liquefying stage and in the maximum pressure loading in [88] originally and an innovative method was proposed.

In the method, an LV sphere model with multi-layers was put forward. In the model, LV and aneurysm shape are always spherical. The LV model yields thick-walled mechanical membrane model. Firstly, it was assumed that the thickness of two segments in the aneurysm remains the same as the remote region during deformation and an incompressible condition is held for the infarcted zone, i.e. the liquid pocket volume is equal to the volume as the muscle. Then, by applying thick-walled mechanical membrane model into two segments in an aneurysm and eliminating the fluid pressure in the infarct, a stress equilibrium equation is achieved [88]. To determine two unknowns, a constitutive law for myocardium is needed, and it was assumed that the total stress in human cardia muscle is a linear function of the muscle length based on experimental data on frog's skeletal muscle during isometric contraction in [91]. Finally, the height factors of an aneurysm for inner and outer segments are calculated from two knowns. For the hypertrophied LV, its height factor is smaller than the normal size LV at the same infarction angle.

The previous model was updated in [92] by removing its two limitations: (1) the centres of two spherical surfaces of the inner or outer segments remain identical during deformation; (2) the segments thickness keeps unchanged. In the updated model the volumes of the inner and outer segments are constant. As a result, there are four unknown angles for the aneurysms. Fortunately, there are four equations as well; one equation is the stress equilibrium equation, and three are the equations based on the incompressible conditions imposed on the inner and outer segments and liquefied infarct. Their detail can be found in [92].

This deformable multi-layer model was extended to an ellipsoidal LV shape but aneurysms on its apex are still spherical in [93]. The stress equilibrium equation and three equations of the incompressible condition for the outer, inner segments and liquefied infarction were derived based on an ellipsoidal LV model. But the idea and method for modelling aneurysm formation remain the same to [92].

4.4 Deformable multi-layer model with isotropic nonlinear myocardium

In Section 4.3, the cardiac muscle constitutive law is regarded as a linear function of LV radius during isometric contraction based on experimental data of frog's skeletal muscle in isometric contraction state. This assumption seems approximate and reasonable. However, if aneurysms are interested to predict during diastole, this linear constitutive relationship will be invalid.

In [94], the aneurysms of two dog LV models were predicted based on a nonlinear passive constitutive law for myocardium during diastole, which reads as:

$$\sigma = A\left(e^{k\varepsilon} - 1\right) \tag{39}$$

where A, k are elastic constants decided from the experimental diastolic p-V curves, ε is the natural strain defined as $\varepsilon = \ln l/l_0$ and l, l_0 are the deformed and reference lengths, respectively.

For the remote myocardium, before an aneurysm occurs, two segment layers are in the ring shapes with radii a, a_1 and b, b_1, respectively, and their stress-strain relationships are written as

$$\begin{cases} \sigma = A\left(e^{k\varepsilon_a} - 1\right), \varepsilon_a = \ln\left[(a + a_1)/(a + a_1)_0\right] \\ \sigma = A\left(e^{k\varepsilon_b} - 1\right), \varepsilon_b = \ln\left[(b + b_1)/(b + b_1)_0\right] \end{cases} \tag{40}$$

where subscript '0' denotes the LV reference configuration (early diastole). After an aneurysm occurs, the stress-strain relationships of the two segment layers are in the following forms

$$\begin{cases} \sigma_\theta = A\left(e^{k\varepsilon_\theta} - 1\right), \varepsilon_\theta = \ln\left[(r + r_1)\theta/(r + r_1)_0\,\theta_0\right] \\ \sigma_\varphi = A\left(e^{k\varepsilon_\varphi} - 1\right), \varepsilon_\varphi = \ln\left[(s + s_1)\varphi/(s + s_1)_0\,\varphi_0\right] \end{cases} \tag{41}$$

Eventually, two ratios σ_θ/σ, σ_φ/σ are expressed by the following equations from Eqs. (40) and (39)

$$\begin{cases} \sigma_\theta/\sigma = \left(e^{k\varepsilon_\theta} - 1\right)/\left(e^{k\varepsilon_a} - 1\right) \\ \sigma_\varphi/\sigma = \left(e^{k\varepsilon_\varphi} - 1\right)/\left(e^{k\varepsilon_b} - 1\right) \end{cases} \tag{42}$$

After Eq. (42) is coupled in the stress equilibrium equation and the LV reference configuration, diastolic *p*-*V* curve, LV wall passive mechanical property constants A, k, damage angle, the equation can be solved along with five incompressible conditions and four geometric relations for ten unknowns numerically and iteratively. The detail of this process is present in [94]. It is demonstrated that an increasing damage angle can result in a significantly rising σ_θ/σ and a dramatical LV wall thinning effect, eventually being favourable to LV rupture.

4.5 Single-layer balloon model with isotropic nonlinear myocardium

When a spherical balloon with rubber-like material, which is subject to a constitutive law in terms of the following strain energy function [95]

$$\psi = a\left(I_1 - 3\right) + b\ln\left[\frac{\left(I_2 - 3\right) + c}{c}\right] + d\left(I_2 - 3\right) \tag{43}$$

where a to d are positive material property constants, I_1 and I_2 are the first two invariants of three principal stretches, λ_1, λ_2 and λ_3, $I_1 = \lambda_1^2 + \lambda_2^2 + \lambda_3^2$, $I_2 = \lambda_1^2\lambda_2^2 + \lambda_2^2\lambda_3^2 + \lambda_1^2\lambda_3^2$; under an increasing transmural pressure, the balloon volume rises with the pressure until λ_1=1.5. Beyond that stretch and until λ_1=3.84, the balloon volume decreases with the pressure. At λ_1>3.84, the balloon volume increases with the pressure once more. Thus, at λ_1=1.5, the balloon exhibits an elastic instability and shows a blowout effect [96].

For a spherical balloon with rubber-like material described by the Ogden type of strain energy function such as

$$\psi = \frac{c}{k}\left(\lambda_1^k + \lambda_2^k + \lambda_3^k - 3\right) \tag{44}$$

when constant k is in the range of (-3/2, 3), at λ_1=1.5, the blowout effect comes to exist as well [97].

In [97], a human LV was considered single-layer membrane sphere with an infarcted zone on top, as shown in Fig. 10a. When the Ogden model Eq. (44) with k =2 was applied, at a certain transmural pressure the infarcted zone can blow out as illustrated in Fig. 10b. For passive human myocardium, the constant is k =18. In this case, the infarcted zone cannot blow out to form an aneurysm during diastole.

During systole, k =18 is applicable to the infarcted region, the remote region can contract to the critical sarcomere length ratio (1.18) against 50, 100 and 150mmHg ESPs, respectively. It is demonstrated that the infarct can blow out to generate an aneurysm, especially at a lower ESP, see Fig. 10c-e. The reason for this effect was that the same active tension was applied to three different ESPs. In the predictions, LVESV enclosed by the remote myocardium should be kept the same by increasing active tension at these different ESPs.

Except the biomechanical property factors shown above, a few parameters such as heart beating rate, myocardium contractility and afterload are related to an aneurysm bulging based on an in vitro experimental study on the bulging in [98], thus, to avoid an aneurysm bulging hemodynamic management may be needed.

4.6 Biomechanical properties of LV aneurysms

LV aneurysm tissue samples of eleven MI patients (nine chronic aneurysms and two acute aneurysms after MI) were studied by using uniaxial tensile test in vitro in [99]. The samples were fibrous, fibrous and muscular, and muscular aneurysms, respectively. The experimental stress-length data were best fitted with the following exponential function

$$\sigma = ae^{b(l-l_1)/l_1} + c \tag{45}$$

where a, b, c are property constants, l_1 is the sample length at 100g/cm^2 stress (1g force), b is used to clarify variations of aneurysm tissue stiffness. For the fibrous, fibrous and muscular, and muscular aneurysms, the mean b values are 130, 28 and 17 in comparison with 32±2 of the mean of seven normal cat papillary muscles [99].

In [100], an axis-symmetrical thick-walled FE model of human LV with a chronic apical aneurysm was established and loaded with a variable LV diastolic pressure increasing from zero to 12mmHg during diastole. The LV wall is an isotropic nonlinear material, and its passive constitutive law is indicated by the following strain energy function [100]

$$\psi = \frac{a}{b^2(1+\nu)}\left\{\sum_{i=1}^{3}\left(\lambda_i^b - 1\right) + \frac{(1-2\nu)}{\nu}\left[\left(\prod_{i=1}^{3}\lambda_i\right)^{\frac{-b\nu}{1-2\nu}} - 1\right]\right\} \tag{46}$$

where a and b are positive property constants, ν is Poisson's ratio for an isotropic material, $\nu = -\ln\lambda_{tr}/\ln\lambda$, λ is the stretch in the direction of uniaxial load, λ_{tr} is the transverse stretch to the direction of uniaxial load. From Eq. (46), the second Poila-Kirchhoff stresses are calculated by

$$S_i = \frac{\partial \psi}{\partial \lambda_i} = \frac{a}{\lambda_i b(1+\nu)}\left\{\lambda_i^b - \left(\prod_{i=1}^{3}\lambda_i\right)^{\frac{-b\nu}{1-2\nu}}\right\} \tag{47}$$

Based on material incompressibility condition, $\lambda\lambda_{tr}\lambda_{tr}$=1, for a uniaxial load, the expression $\prod_{i=1}^{3}\lambda_i = \lambda^{1-2\nu}$ should be held. Then, the first principal Cauchy stress under uniaxial load is expressed in terms of the following expression

$$\sigma = \lambda S = \frac{a}{b(1+\nu)}\left\{\lambda^b - \lambda^{-b\nu}\right\} \tag{48}$$

where the material property constants a and b were best fitted by using uniaxial test data for aneurysm tissues [100], and the measured p-V curve of healthy human LVs based on a spherical LV model [101]. These constants were assigned to the MI zone and remote zone, respectively, in the FE model, while ν=0.45 was applied to both the zones. p-V curves were extracted from results predicted by FEA. It was identified that the curves are shifted substantially to the left of the normal p-V curve, and their slope increases with aneurysm size.

MRI images of a sheep LV were taken at 10wk after MI with aneurysm, a FE model was generated by fitting eight short-axis and four long-axis MRI image slices at the start of diastole. The passive and active constitutive laws in Eqs. (20), (25)-(27) were applied to the remote, border and aneurysm zones with different constants C and σ_{amax} but the same b_f, b_s and b_{fs}. The FE model was loaded with 7.5mmHg LVEDP and 60mmHg end-isometric contraction LV pressure with a set of temporary c and σ_{amax}. Two LV configurations at ED and end-isometric contraction were compared with the corresponding LV configurations extracted from MRI images to get an error between them. Then c and σ_{amax} were altered and a new FEA was launched to check the error, such a cycle was repeated until a reasonable error achieved [56].

It was indicated that only when σ_{amax} of the border zone was reduced by 50% the observed stretching of border fibres in isometric contraction can be reproduced. c of the passive aneurysm has little effect on isometric contraction of border zone. This suggests that contraction dysfunction in border zone is responsible for the myocardium contractile dysfunction [56].

The passive and active constitutive laws in Eqs. (20), (25)-(27) have been applied to investigate the diastolic stiffness necessary condition under which MI achieve akinesis in [102], to calculate stress in an ovine LV with aneurysm in [103], to simulate surgical anterior ventricular restoration (SAVER) operation on a sheep LV with aneurysm in [104], to clarify stress level in nine sheep LVs after linear

repair of their LV aneurysms in [105], to optimize the algorithm for efficiently determining the maximum active tensions in remote and border zones in [106] and to decide the optimum material injecting locations in a LV with aneurysm in [107,108]. Recently, they were employed to identify temporal changes in material properties in MI zone based on late gadolinium enhancement (LEG)-MRI images of the pig LV at the baseline, 1, 4, 8 and 12wk after MI in [109]. The properties in vivo assessment agreed well with the ex-vivo biaxial tensile tests.

5 Growth modelling after MI

Living soft tissue can increase its mass and change its biomechanical property to respond to an altered environment from a biomechanical point of view [110]. The mass change is related to growth after MI and the biomechanical property alternation is concerned in remodelling process. Myofibre and fibroblast can grow and remodel themselves when the environment which relies on varies, for example aging and disease. Additionally, tissue fibre orientation and microstructure can adapt during cardiac growth and remodelling as well [111-113]. After MI, the collagen fibre growth and remodelling are critical for MI healing and LV pumping function recovery. The modelling of growth and remodelling can be useful for understanding of healing mechanism and assessment of LV pumping function.

5.1 Collagen concentration post-MI

After MI extracellular matrix (ECM) turnover exists, including ECM construction and destruction. Macrophage plays a critical role in regulation of ECM turnover. In the regulation, macrophage not only releases transforming growing factor β (TGF-β) to stimulate fibroblasts for producing collagen fibres, but also secretes matrix metalloproteinases (MMPs) or tissue inhibitor of metalloproteinases (TIMPs) to degrade the collagen fibres [114-118]. If ECM construction and destruction are imbalance, congestive heart failure, LV aneurysm, rupture and so on can be present, as seen in Fig. 11a [119].

Key factors regulating ECM were identified experimentally by examining the most significant variations in ECM gene expression in MI region in comparison with gene expression in remote region at 1wk after MI and in normal LV of the control group in [120]. These key factors identified include macrophage, fibroblast, TGF-β, MMP-9 and collagen I. The regulating mechanism and pathways for these factors to control collagen construction and destruction are illustrated in Fig. 11b. The ordinary differential equations (ODE) for macrophage, TGF-β, fibroblast, activated MMP-9, bound MMP-9 and collagen fibre concentrations are expressed as [120]

$$\begin{cases} \frac{dM_\phi}{dt} = M(T_\beta) - d_{M_\phi} \times M_\phi \\ \frac{dT_\beta}{dt} = k_{M_\phi T} \times M_\phi + k_{FT} \times F + u_T - d_{T_\beta} \times T_\beta \\ \frac{dF}{dt} = k_F \times F_g(T_\beta) \times F \times (1 - k_{cr}) - d_F \times F \\ \frac{d[CM_9]}{dt} = k_{on} \times M_{9A} \times C - k_{onc} \times [CM_9] \\ \frac{dM_{9A}}{dt} = k_{M_\phi M_9} \times M_\phi \times H(T_\beta) + k_{off} \times [CM_9] - k_{on} \times M_{9A} \times C - d_{M_9} \times M_{9A} \\ \frac{dC}{dt} = k_{FC} \times F \times F_C(T_\beta) \times F_C(C) + k_{off} \times [CM_9] - k_{on} \times M_{9A} \times C \end{cases} \quad (49)$$

where M, M_ϕ, T_β, F, $[CM_9]$, M_{9A} and C stand for the concentrations of monocyte, macrophage, TGF-β, fibroblast, bound MMP-9, activated MMP-9 and collagen fibre, respectively; k_{M_ϕ}, $k_{M_\phi T}$, k_F, k_{FT}, k_{on}, k_{onc}, $k_{M_\phi M_9}$, k_{off} and k_{FC} are known chemical reaction rate constants; d_{M_ϕ}, d_{T_β}, d_F and d_{M_9} are known degradation rate constants; u_T is MI scar size; $F_g(T_\beta)$, $F_C(T_\beta)$, $F_C(C)$ and $H(T_\beta)$ are known empirical correlations; $k_{cr} = k_m + M_\phi/\rho_{M_\phi} + F/\rho_F + C/\rho_C$, ρ_{M_ϕ}, ρ_F and ρ_C are the maximal density of macrophage, fibroblast and collagen fibre, k_m is the rate of myocyte death $k_m = 0.17 + 0.56e^{-d_m t}$, d_m=0.05 [120].

The ODEs in Eq. (49) were solved in MATLAB for variables M_ϕ, T_β, F, M_{9A}, $[CM_9]$ and C under an initial boundary condition and with related rate constants. Effects of intervention applied to MI at different MI ages on collagen concentration were evaluated by using the model. The intervention applied at 1wk post-MI can archive the best collagen concentration profile from 2wk after MI [120].

5.2 Fibroblast growth modelling

Inflammation, tissues formation, angiogenesis, tissue contraction and tissue remodelling usually occur in sequence during the dermal healing process in injured skin. The interaction between ECM and fibroblasts, which are the cells in 100μm length forming collagen fibres in 1μm in diameter, is one key event in the process [121]. After the blood clot being formed during the inflammation, white blood cells entre the wound zone, then fibroblasts migrate into the zone and start replacing the clot with collagen fibres and new tissue is generated. After the new tissue has been remodelled, a scar is formed.

A few interactions between EMC and fibroblast exist in the healing process. Fibroblast movement is guided by the orientation of EMC and collagen fibrils are formed by procollagen molecules released from the cell surface of fibroblasts [121]. Obviously, wound healing process modelling is essentially to model the orientation of moving fibroblasts by considering the interactions between EMC and fibroblast. A 2D multiscale orientation model was developed in [121] based on continuum EMC and discrete fibroblast cells.

This mathematical model was extended into a 2D multiscale model for MI healing process in [122] by considering collagen fibre mean orientation and area fraction based on experimental results of cryo-infarct scars [123]. The model includes three sub-models for fibroblast generation, fibroblast orientation and collagen fibre growth. It was assumed that fibroblast migration speed, proliferation, rate,

collagen deposition rate, and collagen degradation rate change with chemokine concentration linearly in the maximum and minimum values [122]. The 2D reaction-diffusion equation of chemokine concentration due to the generation of inflammation is written as

$$D_c \nabla^2 C_c = \begin{cases} k_{c,\deg} C_c - k_{c,\text{gen}}, & \text{in MI} \\ k_{c,\deg} C_c, & \text{outside MI(in remote)} \end{cases} \tag{50}$$

where D_c is chemokine diffusion coefficient, C_c is chemokine concentration, $k_{c,\deg}$ is chemokine degradation coefficient, $k_{c,gen}$ is chemokine generation coefficient.

Once MI occurs, myocardium strain components in MI region will differ from those in the remote region and be subject to a considerable variation across the border between two regions. The strain field is continuous across the border and described by a cumulative normal distribution with a standard deviation of 0.08 as follows:

$$\varepsilon(r,\theta) = \varepsilon_{\text{MI}} + \frac{(\varepsilon_{\text{remote}} - \varepsilon_{\text{MI}})}{\chi_\varepsilon \sqrt{2\pi}} \int_{-\infty}^{r} e^{-\frac{[r - r_{MI}(\theta)]^2}{2\chi_\varepsilon^2}} dr \tag{51}$$

where $\varepsilon(r,\theta)$ is a strain component in MI region, $\varepsilon_{\text{remote}}$ and ε_{MI} are strain components in the remote and the centre of MI, respectively, $\varepsilon_{\text{remote}}$ =-0.05 in the circumferential and longitudinal directions, ε_{MI} =0.05 in the two directions (biaxial case) or 0.05(circumferential) and 0(longitudinal) (uniaxial case) [122], $r_{MI}(r)$ is the radius of MI border, and χ_ε is standard deviation for specifying the width of strain transition across the border, χ_ε =0.08.

Fibroblasts were considered discrete discs in 5μm radius and their orientation vector $\vec{\rho}$ was decided probabilistically by cues such as chemokine concentration gradient, strain anisotropy, fibre alignment and existing fibroblast orientation. $\vec{v}$ depends on individual orientation vector $\overrightarrow{c_\iota}$ of the cues, and fibroblast orientation:

$$\vec{v}(\varphi) = \frac{\sum \overrightarrow{c_\iota}}{\iota + \sum \|\overrightarrow{v}\|}, \varphi(\theta_{\text{cf}}; \overline{\theta}_{\text{cf}}, \chi_{\text{cf}}) = \frac{1}{\chi_{\text{cf}}\sqrt{2\pi}} \sum_{n=-\infty}^{\infty} e^{-\frac{(\theta_{\text{cf}} - \overline{\theta}_{\text{cf}} + 2\pi n)}{2\chi_{\text{cf}}^2}}, \chi_{\text{cf}} = -2\ln\|\vec{v}\|, \theta_{\text{cf}} \in [-\pi, \pi] \tag{52}$$

where $\vec{c}_i$ is weighted and normalized individual cue orientation vector, ι is persistence turning factor for the existing orientation of fibroblasts, ι should ensure $\ln\|\vec{v}\| < 1$, $\varphi(\theta_{\text{cf}}; \overline{\theta}_{\text{cf}}, \chi_{\text{cf}})$ is wrapped normal probability density function, θ_{cf} is orientation angle, $\overline{\theta}_{\text{cf}}$ is mean orientation, χ_{cf} is orientation standard deviation.

Collagen fibres in the EMC of the cell where fibroblasts are located can be degraded, deposited and rotated to realize remodelling process. Fibroblasts degrade the fibres at a rate related to the local collagen and chemokine concentrations and deposit the fibres along the current cell orientation at a rate as a function of local chemokine concentration. Fibroblasts rotate the fibres toward parallel the current cell orientation at a rate as a function of difference between the cell and the collagen fibre orientations. The equations for the degradation, deposition and rotation are written as

$$\frac{dN_{\mathrm{cf}}}{dt} = k_{\mathrm{cf,gen}}(C_c)\zeta\pi R_{\mathrm{cell}}^2\delta(\theta_{\mathrm{cell}}) - k_{\mathrm{cf,deg}}(C_c)N_{\mathrm{cf}} \tag{53}$$

and

$$\frac{d\theta_{\mathrm{cf}}}{dt} = \begin{cases} k_{\mathrm{cf,rot}}\|sin(\theta_{\mathrm{cell}} - \theta_{\mathrm{cf}})\|, \theta_{\mathrm{cell}} - \theta_{\mathrm{cf}} \text{ in quadrants I and III} \\ -k_{\mathrm{cf,rot}}\|sin(\theta_{\mathrm{cell}} - \theta_{\mathrm{cf}})\|, \theta_{\mathrm{cell}} - \theta_{\mathrm{cf}} \text{ in quadrants II and IV} \end{cases} \tag{54}$$

where N_{cf} is number of collagen fibres in the fibroblast cell boundary, $k_{\mathrm{cf,gen}}(C_c)$ is collagen fibre generation rate, ζ is the estimated maximum number of collagen fibres per unit area, 14000fibers/μm^2, R_{cell} is the radius of a fibroblast, $\delta(\theta_{cell})$ is delta function enforcing collagen fibres deposition along the cell orientation only, θ_{cell} is fibroblast cell orientation, $k_{\mathrm{cf,deg}}(C_c)$ is collagen fibre degradation rate coefficient. Non-collagen fibres have not deposition but degradation and modelled by

$$\frac{dN_{\mathrm{ncf}}}{dt} = -k_{\mathrm{ncf,deg}}(C_c)N_{\mathrm{ncf}} \tag{55}$$

where N_{ncf} is number of non-collagen fibres in a fibroblast cell, $k_{\mathrm{ncf,deg}}(C_c)$ is non-collagen fibre degradation rate coefficient. The model of Eqs. (50)-(55) was called the agent-based model in [122].

The determination of the model coefficients in Eqs. (50)-(55) and numerical method for solving the equations can be found in [122]. Under the equal-biaxial condition, the collagen fibre orientation is random without dominant direction. Under the uniaxial condition, however, a dominant orientation occurs. These results suggest that the mechanical stimuli can modulate MI healing pattern. More results of collagen fibre growth pattern during MI healing process can be found in [124].

5.3 Coupled fibroblast growth and microstructure-based modelling

The first multiscale model. i.e. agent-based model was established for collagen fibre growth in MI scar healing process. The model was coupled with finite element model (FEM) to predict the scar fibre structure after MI in [125]. A squared scar patch with 100μm length and width is isolated on the epicardium of an LV and modelled. FEM was accommodated in an open source code-FEBio developed by the University of Utah. The strain energy function for the incompressible scar tissue was originated from [81] but with some modifications and is written as

$$\begin{cases} \psi = \frac{1}{2}b_1\left(e^q - 1\right) + b_2\left(I_1 - 3\right) \\ q = b_3\left(b_4E_{11}^2 + b_5E_{22}^2 + b_6E_{33}^2 + 4b_7E_{12}^2 + 4b_8E_{23}^2 + 4b_9E_{31}^2\right) \end{cases} \tag{56}$$

where b_1 to b_9 are positive model constants, I_1 is the first invariant of the right Cauchy–Green deformation tensor, E_{ij} are Lagrange finite strain tensor components, subscripts 1, 2 and 3 specify the circumferential, longitudinal and radial directions, respectively; b_4 to b_9 are model constants relating to collagen fibre orientation and calculated by the following expressions

$$\begin{cases} b_4 = k_{\mathrm{cf}}\sum_{i=1}^{N_{\mathrm{cf}}}\cos^4\phi_{\mathrm{cfi}}\cos^4\theta_{\mathrm{cfi}}, b_5 = k_{\mathrm{cf}}\sum_{i=1}^{N_{\mathrm{cf}}}\cos^4\phi_{\mathrm{cfi}}\sin^4\theta_{\mathrm{cfi}}, b_6 = k_{\mathrm{cf}}\sum_{i=1}^{N_{\mathrm{cf}}}\sin^4\phi_{\mathrm{cfi}} \\ b_7 = k_{\mathrm{cf}}\sum_{i=1}^{N_{\mathrm{cf}}}\cos^4\phi_{\mathrm{cfi}}\cos^2\theta_{\mathrm{cfi}}\sin^2\theta_{\mathrm{cfi}}, b_8 = k_{\mathrm{cf}}\sum_{i=1}^{N_{\mathrm{cf}}}\cos^2\phi_{\mathrm{cfi}}\sin^2\phi_{\mathrm{cfi}}\sin^2\theta_{\mathrm{cfi}}, b_9 = k_{\mathrm{cf}}\sum_{i=1}^{N_{\mathrm{cf}}}\cos^2\phi_{\mathrm{cfi}}\sin^2\phi_{\mathrm{cfi}}\cos^2\theta_{\mathrm{cfi}} \end{cases} \tag{57}$$

where k_{cf} is collagen fibre stiffness, N_{cf} is number of collagen fibres, θ_{cf} is fibre azimuth angle, $\theta_{\mathrm{cf}} \in [-\pi, +\pi]$, ϕ_{cf} is zenith angle, $\phi_{\mathrm{cf}} \in [-\pi/2, +\pi/2]$. In the model, b_6, b_8 and b_9 are negligible small. The results showed that fibroblasts alignment in the orientation of the greatest strain/stretch can reduce the level of anisotropy of collagen fibres in the scar.

The 2D planar agent-model presented in Section 4.2 was extended into 3D spherical agent-model in [126]. The biomechanical model was a simplified version by keeping the first two terms in the constitutive law for passive myocardium in [61]. In the remote region, the strain energy density function under incompressible condition reads as

$$\psi = \frac{a}{2b}\left[e^{b(I_1-3)} - 1\right] + \frac{a_{\mathrm{cf}}}{2b_{cf}}\left\{e^{b_{\mathrm{cf}}[I_4(\theta_{\mathrm{cf}})-1]^2} - 1\right\} \tag{58}$$

where a, b,a_{cf} and b_{cf} are model parameters, I_1 and $I_4(\theta_{\mathrm{cf}})$ are invariants of the right Cauchy-Green tensor.

Collagen fibre volume fraction V_{cf} and fibre orientation density function in MI region are involved to reflect the growth of MI scar and the change in fibre orientation and are updated by using the agent-model. The corresponding strain energy function is modified as follows

$$\psi = (1-V_{\mathrm{cf}})\frac{a}{2b}\left[e^{b(I_1-3)} - 1\right] + V_{\mathrm{cf}}\frac{a_{\mathrm{cf}}}{2b_{\mathrm{cf}}}\int_{I_4(\theta_{\mathrm{cf}})\geq 1}\left\{e^{b_{\mathrm{cf}}[I_4(\theta_{\mathrm{cf}})-1]^2} - 1\right\}\frac{N_{\mathrm{cf}}(\theta_{\mathrm{cf}})}{N_{\mathrm{cft}}}d\theta_{\mathrm{cf}} \tag{59}$$

where N_{cft} is total number of collagen fibres at a time, the integral is operated when $I_4(\theta_{\mathrm{cf}}) \geq 1$, otherwise the fibres are not in engagement.

The biomechanical model above was coupled the agent-model by employing idealized rat LV with circular and elliptical disc shaped MI at ED and solved in finite element analysis program (FEAP) (University of California at Berkeley). The collagen fibre structure in the LV wall was generated by using the method for myofibres. The predicted results illustrated that MI shape can affect collagen fibre structure during scar healing process.

Note that in the remote region, the LV tissue should be healthy myocardium rather than collagen fibres specified in the model Eq. (59), thus, a_{cf} and b_{cf} in the equation should be in terms of healthy myocardium. In the MI region, a_{cf} and b_{cf} are the model constants for collagen fibres.

5.4 Growth modelling of along myofibre orientation

In [127], the remodelling process of an LV after MI was regarded as an isochoric myofibre growth process where growth is along the fibre orientation $\boldsymbol{f}_0$ but shrinks in the cross-fibre direction $\boldsymbol{s}_0$ and remains unaffected in the sheet normal direction $\boldsymbol{n}_0$ in passive state. Then the growth deformation gradient tensor is expressed by

$$\boldsymbol{F}^g = l\,\boldsymbol{f}_0 \otimes \boldsymbol{f}_0 + \frac{1}{l}\boldsymbol{s}_0 \otimes \boldsymbol{s}_0 + \boldsymbol{n}_0 \otimes \boldsymbol{n}_0 \tag{60}$$

where l is a scalar growth variable that was driven by the Cauchy stress along the myofibre, and its change rate is determined by a growth function and an empirical criterion [127]

$$\frac{dl}{dt} = \frac{1}{t_l}\left(\frac{l_{max} - l}{l_{max} - 1}\right)^m \max\left[tr(\sigma) - \sigma^{crit}, 0\right] \tag{61}$$

where l_{max} is the maximum sarcomere lengthening, m is a power, t_l is adaptation rate, σ^{crit} is the stress threshold for growth, $tr(\sigma)$ is the trace of the Cauchy stress tensor, $\sigma = \boldsymbol{F}^e \boldsymbol{S}^e \boldsymbol{F}^{et}$, $\boldsymbol{F}^e$ is the deformation gradient tensor of elastic part, $\boldsymbol{S}^e$ is the second Piola stress tensor calculated by the strain energy function, Eq. (20), in terms of the elastic Green-Lagrange strain tensor $\boldsymbol{E}^e = 0.5\left(\boldsymbol{F}^{eT}\boldsymbol{F}^e - \boldsymbol{I}\right)$, $\boldsymbol{I}$ is the unit tensor.

This growth model was involved into LS-DYNA to predict myofibre growth in a patient-specific LV geometry in two cases: one is cardiac growth with MI, the other one is cardiac growth after MI was removed surgically. The results agreed conceptually with clinical observations and an LV with the removed infarcted zone didn't recline the driving force for myocardium growth or remodelling. However, the model is challenged with that cardiac growth in MI region is collagen growth rather than myofibre growth. How to make the model applicable to the collagen growth is not included in [127].

5.5 Growth modelling of LV along two orientations

In [128], the model for cardiac growth after MI above was extended in the sheet direction to involve LV wall thinning effect by considering myocyte death due to a short supply in oxygen (O_2) concentration c_{O_2} after MI in passive state. The ODE for c_{O_2} concentration diffusion in myocardium is written as

$$\frac{dc_{O_2}}{dt} = \nabla \cdot \boldsymbol{q}_{O_2} + Q_{O_2} \tag{62}$$

where $\boldsymbol{q}_{O_2}$ is the diffusion flux in the myocardium, $\boldsymbol{q}_{O_2} = -D_{O_2}\nabla c_{O_2}$, D_{O_2} is the diffusion coefficient, Q_{O_2} is the O_2 source. The growth deformation gradient tensor for LV wall thinning is expressed by

$$\boldsymbol{F}^g = \boldsymbol{I} + \left(l_s - 1\right)\boldsymbol{n_0} \otimes \boldsymbol{n_0} \tag{63}$$

where l_s is the scalar growth variable in the sheet direction, and is driven by c_{O_2} in the following form [128]

$$\frac{dl_s}{dt} = \frac{1}{t_{l_s}}\left(\frac{l_s - l_{smin}}{1 - l_{smin}}\right)^{m_s}\left(c_{O_2} - 1\right) \tag{64}$$

where t_{l_s}, l_{smin} and m_s are the model constants.

Collagen fibre degradation concentration c_{col} is due to changes in metalloproteinase concentration c_{MMP}, and reads as [128]

$$\begin{cases} \dfrac{dc_{MMP}}{dt} = \left(\dfrac{c_{MMP}}{c_{MMP}^{in}} \right)^{-m} \left(1 - c_{O_2} \right) \\ \dfrac{dc_{col}}{dt} = a_{MMP} \dfrac{dc_{MMP}}{dt} \end{cases} \tag{65}$$

where m and a_{MMP} are the model constants, c_{MMP}^{in} is the initial c_{MMP}. Collagen fibre destruction makes LV in dilatation. Then a growth deformation gradient tensor and its corresponding scalar growth variable in the myofibre direction are present as follows

$$\begin{cases} \boldsymbol{F}^{g} = \boldsymbol{I} + \left(l_{\mathrm{f}} - 1 \right) \mathrm{f}_0 \otimes \mathrm{f}_0 \\ \dfrac{dl_{\mathrm{f}}}{dt} = \dfrac{1}{t_{l_{\mathrm{f}}}} \left(\dfrac{l_{\mathrm{f}\,max} - l}{l_{\mathrm{f}\,max} - 1} \right)^{m_{\mathrm{f}}} \left(1 - c_{O_2} \right) \end{cases} \tag{66}$$

where $t_{l_{\mathrm{f}}}$, $l_{\mathrm{f}\,max}$ and m_{f} are the model constants.

The strain energy function for passive myocardium in [61] was used as biomechanical model for LV wall with MI. These models above were embedded in Abaqus. This growth model has provided an insight into LV remodelling after MI by integrating chemical reactions and biomechanical models for passive myocardium.

5.6 Integrated electromechanical volumetric growth modelling

An integrated electro-mechanical-growth LV model was put forward to simulate cardiac therapies after MI [129]. The integrated model includes two sub-models, namely the LV wall volumetric growth model and electro-mechanical model. In the volumetric growth model, an increased or a reduced cyclical LVEDP was applied to induce a growth (increase in LV chamber and wall volumes) or reverse growth (shrinkage in LV chamber and wall volumes) [130].

In the electro-mechanical model, the myocyte electric model for transmembrane voltage, transmembrane and intracellular ion currents, calcium binding to troponin C and exposure of cross-bridge binding sites in [131,132] and the biomechanical model for passive LV wall in Eq. (20) are linked together by the total Cauchy stress along myofiber

$$\boldsymbol{\sigma} = \boldsymbol{\sigma}_p + \boldsymbol{\sigma}_a \left(\boldsymbol{S}, \lambda_{\mathrm{f}}, d\lambda_{\mathrm{f}}/dt, \boldsymbol{\sigma}_{a\,max} \right) \tag{67}$$

where $\boldsymbol{S}$ is cellular state vector related to the ion cycling and contracting force generate in myocytes and serves as the coupling variable between electrophysiology and biomechanics.

The issues on separation of the timescale between growth and elastic deformation, elasticity tensor transformation and residual stress release were explained [129]. Since the whole LV *p-V* loop was simulated, the Windkessel model and aortic valve function were involved to establish a cardiac cycle.

Note that the integrated electro-mechanical-growth model proposed in [129] is only for the myocardium in the remote and border zone. There is just a $0.5\sigma_{\mathrm{amax}}$ active tension on the border zone. In the MI region, there is no active tension and no growth, but c value in Eq. (20) of the passive

biomechanical model can be altered in the simulations [129] to show the stiffness in biomechanical property from the remote region. It was shown that a stiffer MI can suppress the right shift of *p*-*V* loop to maintain the normal LV pumping function. In fact, the growth and remodelling and collagen fibre orientation variation in MI region are not tackled in [129].

6 Discussion and perspective

In this article, mathematical models and modelling methods in biomechanics of infarcted LVs have been summarized and reviewed in detail, especially some comments were provided to them. Such a review has not been seen in the literature so far. The reviewed models span basic *p*-*V* and stress-stretch models to quite complicated integrated growth-electro-mechanical model via comprehensive cardiovascular system model. These models have performed a critical role in understanding of remodelling process after MI and assessment of treatment methods with MI as well as exploration of new therapy techniques for MI treatment. In consequence, excellent outcomes have been achieved, especially after 2000's. Regarding to the limitations in these models, a few suggestions are drawn.

In the cardiovascular system model with MI effects [14], MI size and compliance have been involved explicitly and the *p*-*V* loops can be estimated before and after MI. However, this model is for bovine cardiovascular system rather than for human cardiovascular system. The model parameters, especially LV elastance and its changes, need to be validated based on clinical data of the human cardiovascular system under heathy and MI conditions. The responses of venous and arterial blood pressure and flow rate to MI remodelling need to be predicted and clarified with the model. The ventricular-arterial interaction post-MI can be studied by employing the model. Influences of haemodynamics on LV remodelling/growth, LV pumping function and LV failure are worthy being considered and investigated in the model.

Recently, myofiber remodelling/growth was predicted under various conditions by using an LV spherical biomechanical model coupled to lumped arterial and venous circulation models along with time-varying LV elastance proposed in [133]. These conditions include myocardial hypertrophy [134], pressure or volume overload following MI [135], and hemodynamic reflex compensation post-MI [136]. Similarly, an ellipsoidal LV model was adopted in [137]. This method takes one advantage such as stress information available compared with [14]. However, the LV biomechanical model is homogenous, and MI cannot be involved into the model as a different structure. If the MI structure is included explicitly, an analytical solution for stresses is impossible, thus FEM and complex constitutive law for passive myocardium have to be secured.

In Fig.6b, the MI scar tissue proves a very different biomechanical behaviour from the existing soft tissue in Fig.6a, i.e. the slope of stress-stretch curve is nonlinear rather than linear. In that case, it is difficult to analytically express the stress-stretch relationship. Therefore, more experimental data at various MI ages are on demand to establish the corresponding biomechanical model for MI scars.

LV aneurysm has been modelled in idealized LV bodies such as sphere or axis-symmetrical structure with isotropic material without myofibre network. Rupture phenomenon and active tension/stress are excluded as well. In the future, these factors are worthy being taken into account in LV aneurysm analysis based on realistic LV geometrical model. Additionally, LV aneurysm should be analysed in a cardiac cycle.

The viscoelasticity of infarcted LV tissue can be altered at MI based on experiments [138]. Unfortunately, this issue has been ignored in biomechanical modelling of biomechanics of infarcted LV so far.

Cardiac rupture is a complication after acute MI and the incidence of the rupture can cause immediate death at a rate of (4-24)% in all infarction deaths [139]. However, this effect and myocardium damage are not modelled based on a biomechanical model presently.

Optimizing collagen fibre orientation in the scar after MI is a good idea [79]. Such a kind of biomechanical model should include the growth effect of collagen fibres in MI zone and the remodelling in myocardium in the remote zone by using MRI image-based reconstructed LV geometrical models in the future.

The myocardium is not considered with a different biomechanical property from the MI scar and the myocardium growth or remodelling is neglected in the existing coupled agent-based models for determining collagen fibre orientation under chemical and mechanical cues [125,126]. Importantly, the model parameters are all from animal models for cryo-infarct scars on the epi-surface of rat LV and whether they are applicable to human LV is unclear currently. Additionally, there is no evidence showing that cryo-infarct scars share the same collagen fibre structure with the normal scars caused from coronary artery blockage.

A substantial effort has been devoted to an integrated electro-mechanical-growth LV model [129], but the collagen fibre growth and remodelling are overlooked. And the corresponding results simulated are not compared with clinical observations quantitatively. Further improvements in these limitations are encouraged.

Biomechanics of infarcted LVs is the subject of the structure, function, kinematics and kinetics of infarcted LVs at the organ, cell and organ levels by making use of experimental and mathematical modelling methods. In the article, solid biomechanics is concerned particularly with application in MI remodelling process. In fact, cardiac electrical activity, electromechanical activity, and haemodynamic CFD in LVs were altered after MI. The investigations in these aspects can serve a critical and useful tool to MI diagnosis and therapy assessment. The typical studies on the identifications of cardiac electrical potential and electromechanical activity as well as CFD simulations of haemodynamics in LVs can be attributed to [140], [141-143] and [144] driven by cine or tagged MRI, respectively. A survey on these subjects is out of scope of the present paper. It is very hopeful that these interesting subjects will be surveyed by other experts in the future.

The regional circumferential strain between ES and ED in endocardium is a sensitive index for remodelling at acute stages of MI based on the layer-specific strain analysis of rat myocardium in vitro [145]. Regional diastolic myocardial strain and strain rate in vivo measured via speckle-tracking echocardiography (STE) decline nonuniformly throughout the myocardium post-MI [146]. Thus, the STE-based quantification of regional and temporal differences in myocardial diastolic strain might be useful for clinical assessment of post-MI remodelling. As a result, a STE regional strain-based inverse problem was proposed to optimise the regional maximum contractile tension profile in 16 regions in a swine healthy LV between ED and ES [147]. It is hopefully the method can be used in LV remodelling prediction post-MI in the future.

7 Concluding remarks

A series of mathematical models and modelling methods in biomechanics of infarcted LVs have been summarized and reviewed. These models were classified into four groups, i.e. cardiovascular system model, biomechanical models, LV aneurysm models and growth models, the features of each model were clarified. Primary idea in each model was detailed and principal equations for the models were illustrated. Discussions on the models have been made and further study issues on them were identified. It was shown that significant improvements in the cardiovascular system model, LV aneurysm model, coupled agent-based models and integrated electro-mechanical-growth LV model are on demand presently. The comparison between model prediction and clinical observation should be quantitative. New stress-stretch models for infarcted LV tissue, collagen fibre orientation optimization in scar, cardiac rupture and tissue damage as well as viscoelastic effect post-MI need to be addressed mathematically in the future. The regional strain-based inverse problems for infarcted LVs are desirable.

Compliance with ethical standards

Conflict of interest

The author declares that he has no conflict of interest.

Ethical approval

This article does not contain any studies with human participants or animals performed by the author.

Reference

[1] http://www.who.int/cardiovascular_diseases/priorities/secondary_prevention/country/en/index1.html.

[2] Bhatnagar P, Wickramasinghe K, Williams J, Rayner M and Townsend N, 2015, The epidemiology of cardiovascular disease in the UK 2014, Heart, 101(15), 1-8.

[3] Richardson W J, Clarke SA, Quinn T A, et al, 2015, Physiological implications of myocardial scar structure, Computational Physiology, 5(4), 1877-1909

[4] Lopez-Perez A, Sebastian R and Ferrero J, Three-dimensional cardiac computational modelling: methods, features and applications, BioMedical Engineering Online, 2015, 14, 35, DOI 10.1186/s12938-015-0033-5

[5] Wang V Y, Nielsen P M and Nash M P, 2015, Image-Based Predictive Modeling of Heart Mechanics, Annual Review of Biomedical Engineering, 17, 351-383

[6] Sack K L, Davies N H, Guccione J M, et al, Personalised computational cardiology: Patient-specific modelling in cardiac mechanics and biomaterial injection therapies for myocardial infarction, Heart Failure Reviews, 2016, 21, 819-826

[7] Voorhees A P and Han H C, 2015, Biomechanics of cardiac function, Computational Physiology, 5(4), 1623-1644

[8] Avazmohammadi R, Soares J S, Li D S, Raut S S, Gorman R C and Sacks M S, 2019, A contemporary look at biomechanical models of myocardium, Annual Review of Biomedical Engineering, 21, 417-42

[9] Yang J H and Saucerman J J, 2011, Computational models reduce complexity and accelerate insight into cardiac signalling networks, Circulation Research, 108(1), 70-84

[10] Zeigler A C, Richardson W J, Holmes J W, et al, 2016, Computational modelling of cardiac fibroblasts and fibrosis, Journal of Molecular and Cellular Cardiology, 93, 73-83

[11] Richardson W J and Holmes J W, 2015, Why infarct expansion such as elusive therapeutic target?, Journal of Cardiovascular Translational Research, 8(7), 421-430

[12] Li W G, Biomechanics of infarcted left ventricle-A review of experiments, Journal of Mechanical Behavior of Biomedical Materials, 2020, 103, 103591

[13] Pfeffer J M, Pfeffer M A, Fletcher P J, et al, Progressive ventricular remodelling in rat with myocardial infarction, American Journal of Physiology-Heart Circulatory Physiology, 1991, 260, H1406-H1414

[14] Pilla J J, Gorman J H and Gorman R C, 2009, Theoretic impact on infarct compliance on left ventricular function, Annals of Thoracic Surgery, 87(3), 803-810

[15] Drzewiecki G M, Pilla J J and Welkowitz W, 1990, Design and control of the atrio-aortic left ventricular assist device based on O_2 consumption, IEEE Transactions on Bio-Medical Engineering, 37(2), 47-55

[16] Suga H, 1971, Theoretical analysis of a left-ventricular pumping model based on the systolic time-varying pressure/volume ratio, IEEE Transactions on Bio-Medical Engineering, 18(1), 47-55

[17] Spotnitz H, Sonnenblick E H and Spiro D, 1966, Relation of ultrastructure to function in the intact heart: sarcomere structure relative to pressure volume curves of intact left ventricles of dog and cat, Circulation Research, 18(1), 49-66

[18] Laks M M, Garner D and Swan H J C, 1967, Volumes and compliances measured simultaneously in the right and left ventricles of the dog, Circulation Research, 20(5), 565-569

[19] Noble M I M, Milne E N C, Goerke R J, et al, 1969, Left ventricular filling and diastolic pressure-volume relations in the conscious dig, Circulation Research, 24(2), 269-283

[20] Diamond G, Forrester J S, Hargis J, et al, 1971, Diastolic pressure-volume relationship in the canine left ventricle, Circulation Research, 29(3), 269-283

[21] Murakami T and Kawai C, 1991, Advances in the understanding of systolic and diastolic functions of the heart, International Journal of Cardiology, 32(2), 149-174

[22] Dodge H T, Hay R E and Sandler H, 1962, Pressure-volume characteristics of the diastolic left ventricle of man with heart disease, American Heart Journal, 64(4), 503-511

[23] Gaasch W H, Levine H J and Quinones M A, et al, 1976, Left ventricular compliance: mechanisms and clinical implications, American Journal of Cardiology, 38(4), 645-653

[24] Mirsky I, 1976, Assessment of passive elastic stiffness of cardiac muscle: mathematical concepts, physiologic and clinical considerations, directions of future research, Progress in Cardiovascular diseases, 18(4), 277-308

[25] Wisenbaugh T, Harlamert E and DeMaria A N, 1990, Relation of left ventricular filling dynamics to alternations in load and compliance in patients with and without pressure-overload hypertrophy, Circulation, 81(1), 101-106

[26] Liu C P, Ting C T, Lawrence W, 1993, Diminished contractile response to increased heart rate in intact human left ventricular hypertrophy, Serial changes in left ventricular relaxation and chamber stiffness after larger myocardial infarction in rats, Circulation, 77(6), 1424-1431

[27] Forrester J S, Diamond G and Parmley W W, et al, 1972, Early increase in left ventricular compliance after myocardial infarction, Journal of Clinical Investigation, 51(3), 598-603

[28] Fletcher P J, Pfeffer J M and Pfeffer M A, 1981, Left ventricular diastolic pressure-volume relations in rats with healed myocardial infarction, Circulation Research, 49(3), 618-626

[29] Diamond G and Forrester J S, 1972, Effect of coronary artery disease and acute myocardial infarction on left ventricular compliance in man, Circulation, 45(1), 11-19

[30] Bogen D K, Rabinowitz S A, Needleman A, et al, 1980, An analysis of the mechanical disadvantage of myocardial infarction in the canine left ventricle, Circulation Research, 47(5), 728-741

[31] Ogden R, 1972, Large deformation isotropic elasticity-on the correlation of theory and experiment for incompressible rubberlike solids, Proceedings of Royal Society of London, Series A, 326(1567), 565-584

[32] Sunagawa K, Maughan W L and Sagawa K, 1983, Effect of regional ischemia on the left ventricular end-systolic pressure-volume relationship of isolated canine hearts, Circulation Research, 52(2), 170-178

[33] Sodums M T, Badke F R, Starling M R, et al, 1984, Evaluation of left ventricular contractile performance utilizing end-systolic pressure-volume relationships in conscious dogs, Circulation Research, 54(6), 731-739

[34] Kass D A, Marino P, Maughan W L, et al, 1989, Determinants of end-systolic pressure-volume relations during acute regional ischemia in situ, Circulation, 80(6), 1783-1794

[35] Nakajima H, Nakajima H O, Hammond R L, et al, 1995, Chronic changes of end-systolic pressure-volume relationship after regional myocardial infarction, Journal of Cardiac Surgery, 10(6), 652-664

[36] Setser R, Henson II R E, Allen J S, et al, 2000, Left ventricular contractility is impaired following myocardial infarction in the pig and rat: assessment by the end systolic pressure–volume relation using a single-beat estimation technique and cine magnetic resonance imaging, Annals of Biomedical Engineering, 28(5), 484-494

[37] Grossman W, Braunwald E, Mann T, et al, 1977, Contractile state of the left ventricle in man as evaluated from end-systolic pressure-volume relations, Circulation, 56(5), 845-852

[38] Mehmel H C, Stokckins B, Ruffmann K, et al, 1981, The linearity of the end-systolic pressure-volume relationship in man and its sensitivity for assessment of left ventricular function, Circulation, 63(6), 1216-1222

[39] Burkhoff D, Si=ugiura S, Yue D T, et al, 1987, Contractility-dependent curvilinearity of end-systolic pressure-volume relations, American Journal of Physiology-Heart Circulation Physiology, 252, H1218-H1227

[40] Kass D A, Beyar R, Lankford E, et al, 1989, Influence of contractile state on curvilinearity of in situ end-systolic pressure-volume relations, Circulation, 79(1), 167-178

[41] Bogen D K, Needleman A and McMahon T A, 1984, An analysis of Myocardial Infarction, Circulation Research, 55(6), 805-815

[42] Perl M, Horowitz A and Sideman S, 1986, Comprehensive model for simulation of left ventricle mechanics, Medical & Biological Engineering & Computing, 24(2), 145-149

[43] Perl M and Horowitz A, 1987, Mechanical model for simulation of ischaemia and infarction of the left ventricle, Medical & Biological Engineering & Computing, 25(3), 284-288

[44] Fung Y C, 1967, Elasticity of soft tissues in simple elongation, American Journal of Physiology, 213(6), 1532-1544

[45] Laird J D and Vellekoop H P, 1977, Time course of passive elasticity of myocardial tissue following experimental infarction in rabbits and its relation to mechanical dysfunction, Circulation Research, 41(5), 715-721

[46] Yettram A L, Vinson C A and Gibson D G, 1979, Influence of the distribution of stiffness in the human left ventricular myocardium shape change in diastole, Medical & Biological Engineering & Computing, 17(5), 553-562

[47] Akaishi M, Weintraub W S, Schneider R M, et al, 1986, Analysis of systolic bulging, Circulation Research, 58(2), 209-217

[48] Fomovsky G M and Holmes J W, 2010, Evolution of scar structure, mechanics, and ventricular function after myocardial infarction in the rat, American Journal of Physiology-Heart and Circulation Physiology, 298(1), H221-H228

[49] Mojsejenko D, McGarvey J R, Dorsey S M, et al, 2015, Estimating passive mechanical properties in a myocardial infarction using MRI and finite element simulations, Biomechanics and Modeling in Mechanobiology, 14(3), 633-647

[50] Guccione J M, McCulloch A D, Waldman L K, 1991, Passive material properties of intact ventricular myocardium determined from a cylindrical model, ASME Journal of Biomechanical Engineering, 113(1), 42-55

[51] Fan L, Yao J, Yang C, et al, Infarcted left ventricles have stiffer material properties and lower stiffness variation: 3D echo-based modeling to quantify in vivo ventricle material properties, ASME Journal of Biomechanical Engineering, 2015, 137(8), 081005

[52] Fan L, Yao J, Yang C, et al, Material stiffness parameters as potential predictors of presence of left ventricle myocardial infarction: 3D echo-based computational modeling study, Biomedical Engineering Online, 2016, 15:34, doi:10.1186/s12938-016-0151-8

[53] Fan L, Yao J, Yang C, et al, Modeling active contraction and relaxation of left ventricle using different zero-load diastole and systole geometries for better material parameter estimation and stress/strain calculations, Molecular & Cellular Biomechanics, 2016, 13(1), 44-68

[54] Hill A V, 1938, The heat of shortening and the dynamic constants in muscle, Proceedings of the Royal Society of London, Series B, 126(843), 136-165

[55] Bovendeerd P H M, Arts T, Delhaas T, et al, 1996, Regional wall mechanics in the ischemic left ventricle: numberical modelling and dog experiments, American Journal of Physiology-Heart and circulation Physiology, 270(1), H398-H410

[56] Guccione J M, Moonly S M, Moustakidis M, et al, 2001, Mechanism underlying mechanical dysfunction in the border zone of left ventricular aneurysm: a finite element model study, Annals of Thoracic Surgery, 71(2), 654-662

[57] Wenk F F, Eslami P, Zhang Z, et al, 2011, A novel method for quantifying the in-vivo mechanical effect of material injected into a myocardial infarction, Annals of Thoracic Surgery, 92(3), 935-941

[58] Fomovsky G M, Macadangdang J R, Aliawadi G, et al, 2011, Model-based design mechanical therapies for myocardial infarction, Journal of Cardiovascular Translational Research, 4(1), 82-91

[59] Gao H, Aderhold A, Mangion K, et al, 2017, Changes and classification in myocardial contractile function in the left ventricle following acute myocardial infarction, Journal of The Royal Society Interface, 14(132), 20170203

[60] Gao H, Mangion K, Carrick D, et al, 2017, Estimating prognosis in patients with acute myocardial infarction using personalized computational heart models, Scientific Reports, 7(1), 13527

[61] Holzapfel G A and Ogden R W, 2009, Constitutive modelling of passive myocardium: a structurally based framework for material characterization, Philosophical Transactions of Royal Society, Series A, 367(1902), 3445-3475

[62] Niederer S A, Hunter P J and Smith N P, 2006, A quantitative analysis of cardiac myocyte relaxation: a simulation study, Biophysical Journal, 90(5), 1697-1727

[63] Beriberoglu E and Goktepe S, 2015, Computational modelling of myocardial infarction, Procedia IUTAM, 12, 52-61

[64] Aliev R and Panfilov A Y, 1996, A simple two-variable model of cardiac excitation, Chaos, Solitons & Fractals, 7(3), 293-301

[65] Goktepe S, Menzel A and Kuhl E, 2014, The generalized Hill model: a kinematic approach towards active muscle contraction, Journal of Mechanics and Physics of Solids, 72, 20-39

[66] Grossman W, Jones D and McLaurin L P, 1975, Wall stress and patterns of hypertrophy in human left ventricle, Journal of Clinical Investigation, 56(1), 56-64

[67] Janz R F, 1982, Estimation of local myocardial stress, American Journal of Physiology-Heart and Circulation Physiology, 242(5), H875-H881

[68] Balzer P, Furber A, Delepine S, et al, 1999, Regional assessment of wall curvature and wall stress in left ventricle with magnetic resonance imaging, American Journal of Physiology-Heart and Circulation Physiology, 277(3), H901-H910

[69] Delepine S, Furber A, Beygui F, et al, 2003, 3-D MRI assessment of regional left ventricular systolic wall stress in patients with reperfused MI, American Journal of Physiology-Heart and Circulation Physiology, 284(4), H1190-H1197

[70] Prunier F, Brette S, Delepine S, et al, 2008, Three-dimensional MRI assessment of regional wall stress after acute myocardial infarction predicts postdischarge cardiac events, Journal of Magnetic Resonance Imaging, 27(3), 516-521

[71] Clerfond G, Biere L, Mateus V, 2015, End-systolic wall stress predicts post-discharge heart failure after acute myocardial infarction, Archives of Cardiovascular Diseases, 108(5), 310-320

[72] Regen D M, Anversa P and Capasso J M, 1993, Segmental calculation of left ventricular wall stresses, American Journal of Physiology-Heart and Circulation Physiology, 264(5), H1411-H1421

[73] Zhong L, Su Y, Gobeawan L, et al, 2011, Progressive left ventricular remodelling and apoptosis late after myocardial infarction in mouse heart, American Journal of Physiology-Heart and Circulation Physiology, 300, H1653-H1660

[74] Zhong L, Su Y, Yeo S Y, et al, 2009, Left ventricular regional wall curvedness and wall stress inpatients with ischemic dilated cardiomyopathy, American Journal of Physiology-Heart and Circulation Physiology, 296(3), H573-H584

[75] Chen C H, Fetics B, Nevo E, et al, 2001, Noninvasive single-beat determination of left ventricular end-systolic elastane in humans, Journal of the American College Cardiology, 38(7), 2028-2034

[76] Hayashida W, Kumada T, Nohara R, et al, 1990, Left ventricular regional wall stress in dilated cardiomyopathy, Circulation, 82(6), 2075-2083

[77] Segar D S, Moran M and Ryan T, 1991, End-systolic regional wall stress-length and stress-shortening relations in an experimental model of normal, ischemic and reperfused myocardium, Journal of American College of Cardiology, 17(2), 1651-1660

[78] Clerfond G, Biere L, Mateus V, et al, 2015, End-systolic wall stress predicts post-discharge heart failure after acute myocardial infarction, Archives of Cardiovascular Disease, 108(5), 310-320

[79] Voorhees A P and Han H C, 2014, A model to determine the effect of collagen fiber alignment on heart function post myocardial infarction, Theoretical Biology and Medical Modelling, 11(6), 1-19

[80] Grytz R and Meschke G, 2009, Constitutive modelling of crimped collagen fibrils in soft tissues, Journal of the Mechanical Behavior of Biomedical Materials, 2(5), 522-533

[81] Costa K D, Holmes J W and McCulloch A D, 2001, Modelling cardiac mechanical properties in three dimensions, Philosophical Transactions of Royal Society Series A, 359(1783), 1233-1250

[82] Korenczuk C E, Barocas V H and Richardson W J, 2019, Effects of collagen heterogeneity on myocardial infarct mechanics in a multiscale fiber network model, ASME Journal of Biomechanical Engineering, 141(9), 091015-1

[83] Witzenburg C M, Dhume R Y, Shah S B, et al, 2017, Failure of the porcine ascending aorta: multidirectional experiments and a unifying microstructural model, ASME Journal of Biomechanical Engineering, 139(3), 031005-1

[84] Dhume R Y, Shih E D and Barocas V H, 2019, Multiscale model of fatigue of collagen gels, Biomechanics and Modeling in Mechanobiology, 18(1), 175-187

[85] Friedman B M and Dunn M I, 1995, Postinfarction ventricular aneurysms, Clinical Cardiology, 18(9), 505-511

[86] Ba'albaki H A and Clements S D, 1989, Left ventricular aneurysms: a review, Clinical Cardiology, 12(1), 5-13

[87] Vayo H W, 1966, The theory of the left ventricular aneurysm, Bulletin of Mathematical Biophysics, 28(3), 363-370

[88] Lowe T E and Love E R, 1948, Cardiac aneurysms-a mechanical analysis of their formation, Australian Journal of Experimental Biology and Medical Science, 26(6), 497-513

[89] Lowe T E and Wartman W B, 1944, Myocardial infarction, British Heart Journal, 6(3), 115-128

[90] Robb J S and Robb R C, 1938, Abnormal distribution of the superficial muscle bundles in the human heart, American Heart Journal, 15(5), 597-603

[91] Evans C L and Hill A V, 1914, The relation of length to tension development and heat production on contraction in muscle, Journal of Physiology, 49(1-2), 10-16

[92] Radhakrishnan S, Ghista D N and Jayaraman G, 1980, Mechanical analysis of the development of left ventricular aneurysms, Journal of Biomechanics, 13(12), 1031-1039

[93] Radhakrishnan S, Ghista D N and Jayaraman G, 1986, Mechanics of left ventricular aneurysm, Journal of Biomedical Engineering, 8(1), 9-23

[94] Mirsky I, McGill P L and Janz R F, 1978, Mechanical behaviour of ventricular aneurysms, Bulletin of Mathematical Biology, 40(4), 451-464

[95] Alexander H, 1968, A constitutive relation for rubber-like materials, International Journal of Engineering Science, 6(9), 549-563

[96] Alexander H, 1971, Tensile instability of initially spherical balloons, International Journal of Engineering Science, 9(1), 151-162

[97] Bogen D K and McMahon T A, 1979, Do cardiac aneurysms blow out?, Biophysical Journal, 27(2), 301-316

[98] Bartel T, Vanheiden H, Schaar J, et al, 2002, Biomechanical modelling of hemodynamic factors determining bulging of ventricular aneurysms, Annals Thoracic Surgery, 74(5), 1581-1587

[99] Parmley W W, Chuck L, Kivowitz C, et al, 1973, In vitro length-tension relations of human ventricular aneurysms, American Journal of Cardiology, 32(7), 889-894

[100] Janz R F and Walderon R J, 1978, Predicted effect of chronic apical aneurysms on the passive stiffness of the human left ventricle, Circulation Research, 42(2), 255-263

[101] Fester A and Samet P, 1974, Passive elasticity of the human left ventricle, Circulation, 50(3), 609-618

[102] Dang A B C, Guccione J M, Mishell J M, et al, 2004, Akinetic myocardial infarcts must contain contracting myocytes: finite-element model study, American Journal of Physiology-Heart and Circulation Physiology, 288(4), H1844-H1850

[103] Walker J C, Ratcliffe M B, Zhang P, et al, 2005, MRI-based finite-element analysis of left ventricular aneurysm, American Journal of Physiology-Heart and Circulation Physiology, 289(2), H1692-H700

[104] Dang A B C, Guccione J M, Zhang P, et al, 2005, Effect of ventricular size and patch stiffness in surgical anterior ventricular restoration: a finite element model study, Annals of Thoracic Surgery, 79(1), 185-193

[105] Walker J C, Ratcliffe M B, Zhang P, et al, 2008, Magnetic resonance imaging-based finite element stress analysis after linear repair of left ventricular aneurysm, Journal of Thoracic and Cardiovascular Surgery, 135(5), 1094-1102

[106] Sun K, Stander N, Jhun C S, et al, 2009, Computationally efficient formal optimization of regional myocardial contractility in a sheep with left ventricular aneurysm, Journal of Biomechanical Engineering, 131(11), 111001-1-10

[107] Wall S T, Walker J C, Healy K E, et al, 2006, Theoretical impact of the injection of material into the myocardium: a finite element model simulation, Circulation, 114(24), 2627-2635

[108] Wenk J F, Wall S T, Peterson R C, et al, 2009, A method for automatically optimizing medical devices for treating heart failure: designing polymeric injection patterns, Journal of Biomechanical Engineering, 131(12), 121011-1-7

[109] McGarvey J R, Mojssejenko D, Shauna M S, et al, 2015, Temporal changes in infarct material properties: an in vitro assessment using magnetic resonance imaging and finite element simulations, Annals of Thoracic Surgery, 100(2), 582-590

[110] Menzel A and Kuhl E, 2012, Frontiers in growth and remodelling, Mechanics Research Communications, 42, 1-14

[111] Bovendeerd P H M, 2012, Modeling of cardiac growth and remodelling of myofiber orientation, Journal of Biomechanics, 45(5), 872-881

[112] Wang V Y, Hussan J R, Yousefi H, et al, 2017, Modelling cardiac tissue growth and remodelling, Journal of Elasticity, 129(1-2), 283-305

[113] Zeigler A C, Richardson W J, Holmes J W, et al, 2016, A computational model of cardiac fibroblast signalling predicts context-dependence drivers of myofibroblast differentiation, Journal of Molecular and Cellular Cardiology, 94, 72-81

[114] Rohde L E, Ducharme A, Arroyo L H, et al, 1999, Matrix metalloproteinase inhibition attenuates early left ventricular enlargement after experimental myocardial infarction in mice, Circulation, 99(23), 3063-3070

[115] MacKenna D, Summerour S R and Villarreal F J, 2000, Role of mechanical factors in modulating cardiac fibroblast function and extracellular matrix synthesis, Cardiovascular Research, 46(2), 257-264

[116] Lindsey M, Wedin K, Brown M D, et al, 2001, Matrix-dependent mechanism of neutrophil-mediated release and activation of matrix metalloproteinase 9 in myocardial ischemia/reperfusion, Circulation, 103(17), 2181-2187

[117] Lindsey M, Escobar G P, Dobrucki L W, et al, 2006, Matrix metalloproteinase-9 gene deletion facilitates angiogenesis after myocardial infarction, American Journal of Physiology-Heart and Circulation Physiology, 290(1), H232-H239

[118] Bujak M and Frangogiannis N G, 2007, The Role of TGF-β signalling in myocardial infarction and cardiac remodeling, Cardiovascular Research, 74(2), 184-195

[119] Zamilpa R and Lindsey M L, 2009, Extracellular matrix turnover and signaling during cardiac remodelling following MI: causes and consequences, Journal of Molecular and Cellular Cardiology, 48(3), 558-563

[120] Jin Y F, Han H C, Berger J, et al, 2011, Combining experimental and mathematical modelling to reveal mechanisms of macrophage-dependent left ventricular remodelling, BMC Systems Biology, 5, 60, doi: 10.1186/1752-0509-5-60

[121] McDougall S, Dallon J, Sherratt J, et al, 2006, Fibroblast migration and collagen deposition during dermal wound healing: mathematical modelling and clinical implications, Philosophical Transactions of the Royal Society, Series A, 364(1843), 1385-1405

[122] Rouillard A D and Holmes J W, 2012, Mechanical regulation of fibroblast migration and collagen remodelling in healing myocardial infarcts, Journal of Physiology, 590(18), 4585-4602

[123] Fomovsky G M, Rouillard A D and Holmes J W, 2012, Regional mechanics determine collagen fiber structure in healing myocardial infarcts, Journal of Molecular and Cellular Cardiology, 52(5), 1083-1090

[124] Richardson W J and. Holmes J W, 2016, Emergence of collagen orientation heterogeneity in healing infarcts and an agent-based model, Biophysical Journal, 110(10), 2266-2277

[125] Rouillard A D and Holmes J W, 2014, Coupled agent-based and finite-element models for predicting scar structure following myocardial infarction, Progress in Biophysics and Molecular Biology, 115(2-3), 235-243

[126] Zhuan X, Luo X Y, Gao H, et al, 2019, Coupled agent-based and hyperplastic modelling of the left ventricle post-myocardial infarction, International Journal for Numerical Methods in Biomedical Engineering, 35(1), e3155

[127] Klepach D, Lee L C, Wenk J F, et al, 2012, Growth and remodelling of the left ventricle: a case study of myocardial infarction and surgical ventricular restoration, Mechanics Research Communications, 42, 134-141

[128] Saez P and Kuhl E, 2016, Computational modelling of acute myocardial infarction, Computer Methods in Biomechanics and Biomedical Engineering, 19(10), 1107-1115

[129] Lee L C, Sundnes J, Genet M, et al, 2016, An integrated electromechanical-growth heart model for simulating cardiac therapies, Biomechanics and Modelling in Mechanobiology, 15(4), 791-893

[130] Lee L C, Genet M, Acevedo-Bolton G, et al, 2015, A computational model that predicts reverse growth in response to mechanical unloading, Biomechanics and Modelling in Mechanobiology, 14(2), 217-229

[131] Wall S T, Guccione J M, Ratcliffe M B, et al, 2012, Electro-mechanical feedback with reduced cellular connectivity alters electrical activity in an infarct injured left ventricle: a finite element model study, American Journal of Physiology-Heart and Circulation Physiology, 302(1), H206–H214

[132] Sundnes J, Wall S T, Osnes H, et al, 2014, Improved discretisation and linearisation of active tension in strongly coupled cardiac electro-mechanics simulations, Computer Methods in Biomechanics and Biomedical Engineering, 17(6), 604–615

[133] Burkhoff D and Tyberg J V, 1993, Why does pulmonary venous pressure rise after onset of LV dysfunction: a theoretical analysis, American Journal of Physiology-Heart and Circulation Physiology, 265, H1818-1828

[134] Witzenburg C M and Holmes J W, 2017, A comparison of phenomenological growth laws for myocardial hypertrophy, Journal of Elasticity, 129(1-2), 257-281

[135] Witzenburg C M and Holmes J W, 2018, Predicting the time course of ventricular dilation and thickening using a rapid compartmental model, Journal of Cardiovascular Translational Research, 11(2), 109-122

[136] Witzenburg C M and Holmes J W, 2019, The impact of hemodynamic reflex compensation following myocardial infarction on subsequent ventricular remodeling, ASME Journal of Biomechanical Engineering, 141, 091010-1

[137] Bozkurt S, 2019, Mathematical modeling of cardiac function to evaluate clinical cases in adults and children, PLoS ONE 14(10): e0224663

[138] Connelly C M, Vogel W M, Wiegner A W, et al, 1985, Effects of reperfusion after coronary artery occlusion on post-infarction scar tissue, Circulation Research, 57(4), 562-577

[139] Kendall R W, DeWood M A, 1978, Postinfarction cardiac rupture: surgical success and review of the literature, Annals of Thoracic Surgery, 25(4), 311-315

[140] Arevalo H J, Vadakkumpadan F, Guallar E, et al, 2016, Arrhythmia risk stratification of patients after myocardial infarction using personalized heart models, Nature Communications, 7(11437), https://doi.org/10.1038/ncomms11437

[141] Sainte-Marie J, Chapelle D, Cimrman R, et al, 2006, Modeling and estimation of the cardiac electromechanical; activity, Computers and Structures, 84, 1743-1759

[142] Sermesant M, Moireau P, Camara O, et al, 2006, Cardiac function estimation from MRI using a heart model and data assimilation: Advances and difficulties, medical Image Analysis, 10, 642-656

[143] Chabiniok R, Moireau P, Lesault P F, et al, 2012, Estimation of tissue contractility from cardiac cine-MRI using a biomechanical heart model, Biomechanics and Modelling in Mechanobiology, 11(5), 609-630

[144] Khalafvand S S, Ng E Y K, Zhong L, et al, 2012, Fluid-dynamics modelling of the human left ventricle with dynamic mesh for normal and myocardial infarction: Preliminary study, Computers in Biology and Medicine, 42, 863-870

[145] Bachner-Hinenzon N, Ertracht O, Malka A, et al, 2012, Layer-specific strain analysis: investigation of regional deformations in a rat model of acute versus chronic myocardial infarction, American Journal of Physiology-Heart and Circulation Physiology, 303, H549-H558

[146] Torres W M, Jacobs J, Doviak H, et al, 2018, Regional and temporal changes in left ventricular strain and stiffness in a porcine model of myocardial infarction, American Journal of Physiology-Heart and Circulation Physiology, 315, H958 –H967

[147] Dabiri Y, Sack K L , Rebelo N, et al, 2019, Method for Calibration of Left Ventricle Material Properties Using Three-Dimensional Echocardiography Endocardial Strains, ASME Journal of Biomechanical Engineering, 141(9), 091007-1 (10 pages)

Table 1 Summary of biomechanical models for LV growth and remodelling after MI

Classification		Contributor	Feature	Ref
Cardiovascular system		Drzewiecki, Pilla and Welkowitz (1990)	1) Venous, pulmonary and arterial systems are represented by fixed compliance and flow resistance. 2) Tricuspid, pulmonary, mitral and aortic valves are modelled with fixed flow resistance and one directional diode. 3) RV and LV are with variable active and passive compliances. 4) In MI zone, there is passive compliance only. 5) The Windkessel model is applied. 6) Compensatory characteristic of the system is considered.	[14]
Biomechanical models of MI	Diastolic *p-V* curve model	Noble, Milne, Goerke, et al (1969) or Diamond G, Forrester, Hargis, et al (1971)	1) LV pressure is as an exponential function of LV chamber volume in diastole or 2) LV pressure is as an exponential function of dimensionless LV chamber volume in diastole.	[19,20]
	Two-parameter Ogden type model	Bogen, Rabinowitz, Needleman, et al (1980)	1) Infarct myocardium is isotropic nonlinear material in diastole and systole. 2) Two-parameter Ogden type strain energy function. 3) LV initial shape is spherical, then deformed into axis-symmetrical shape in diastole and systole. 4) Two parameters are altered to represent MI size effect and passive and active states.	[30]
	Analytical LV model with MI	Sunagawa, Maughan and Sagawa (1983)	1) No border zone. 2) Remote zone and MI zone are considered two separated chambers with the same LV pressure. 3) Three ESPVRs each for remote zone, MI zone and intact LV with MI.	[32]
	Two-parameter Ogden type model with empirical contractility	Bogen, Needleman and McMahon (1984)	1) Two-parameter Ogden type strain energy function. 2) LV initial shape is spherical, then deformed into axis-symmetrical shape in diastole and systole. 3) Two parameters are assigned to healthy myocardium and MI region. 4) Different contraction constants are given to reflect defeated contractility in remote region.	[41]
	Empirical stress-stretch and active tension model	Perl M and Horowitz (1984)	1) Empirical exponential stress-stretch relationship. 2) Empirical active tension with a variable coefficient with cardiac time. 3) *p-V* loop is modelled.	[42]
	Empirical tension-stretch relation	Laird and Vellekoop (1977)	Fung type exponential tension-stretch formula is used to fit MI tissue.	[45]
		Akaishi, Weintraub, Schneider, et al (1986)	An exponential tension-stretch expression is used.	[47]
	Isotropic collagen fibre MI scar	Fomovsky, Rouillard and Holmes (2012)	1) Collagen fibres have not dominant fibre orientation. 2) MI scar is planar and isotropic.	[48]

Table 1 Summary of biomechanical models for LV growth and remodelling after MI (continued)

Classification		Contributor	Feature	Ref
Biomechanical models of MI	Fung type strain energy function for anisotropic myocardium	Guccione, McCulloch, Waldman (1991)	1) Fung type strain energy function in passive state is adopted. 2) In-plane anisotropic but transversely isotropic. 3) Four model constants are determined with *p*, *V* values at ED.	[50]
	Mooney-Rivlin type strain energy function for anisotropic myocardium	Fan et al, (2015,2016)	1 Mooney-Rivlin type strain energy function in passive state is updated. 2) In-plane anisotropic but transversely isotropic 3) Non-MI regional effect. 4) Five model constants are decided by *p*, *V* values at ED.	[51-53]
	Empirical active stress relation based on Hill's model	Bovendeerd, Arts, Delhaas, et al (1996)	1) Hill's three-element active model for myocardium is involved. 2) Three correlations are generated to calculate the active tension.	[55]
	Empirical active stress relation based calcium concentration	Guccione, Moonly, Moustakidis M, et al (2001)	1) LV aneurysm is rigid and un-deformable. 2) LV is a spherical membrane. 3) LV chamber volumes are modelled at ED and ES.	[56]
	Myofibre structure myocardium with active tension model	Gao, Aderhold, Mangion, et al (2017), Gao, Mangion, Carrick, et al (2017)	1) Holzapfel and Ogden (2009) model is used for passive myocardium. 2) Niederer, Hunter and Smith (2006) model is specified for active myocardium. 3) IB/FE methods are combined.	[59,60]
	Myofibre structure myocardium with general Hill model and electro-mechanics coupling	Beriberoglu and Goktepe (2015)	1) Holzapfel and Ogden (2009) model is included for passive myocardium. 2) Generalized Hill model of Goktepe, Menzel and Kuhl (2014) is involved. 3) Aliev and Panfilov (1996) electrophysiological model is considered. 4) Signorini's model is applied to estimate LV pressure. 5) *p-V* loop is modelled.	[63]
	Regional stress model	Grossman, Jones and McLaurin (1975)	1) LV is thick-walled membrane ellipsoid. 2) Meridional radius of curvature in LV endocardium is used. 3) The stress calculated is mean longitudinal stress.	[66]
		Janz (1982)	1) LV is thick-walled membrane ellipsoid. 2) Circumferential and longitudinal stresses are mean values across LV wall. 3) Circumferential and meridional radii of curvature in LV endocardium are used.	[67]
		Regen, Anversa and Capssso (1993)	1) LV is thin-walled membrane ellipsoid with Laplace's law. 2) LV wall stresses are calculated using circumferential and meridional radii of curvatures of LV middle wall profile.	[72]
		Zhong, Su Y, Yeo, et al (2009), Zhong, Su, Gobeawan L, et al (2011)	1) LV wall curvatures and wall thickness are determined from MRI images. 2) LV wall stress is calculated by using meridional radius of curvature of LV middle wall profile.	[73,74]
	Collagen fibre orientation alternation model in MI scar	Voorhees and Han (2014)	1) Collagen fibres are composed of collagen fibrils. 2) Collagen fibrils in MI scar are modelled with crimped model of Grytz and Meschke (2009). 3) Passive myocardium is modelled with Guccione McCulloch and Waldman (1991) model. 4) LV shape is cylindrical and composed of three healthy myocardium patches and one scar.	[79]

Table 1 Summary of biomechanical models for LV growth and remodelling after MI (continued)

Classification		Contributor	Feature	Ref
Biomechanical models of MI	MI scar model with transmurally variable orientation of large collagen fibres	Costa, Holmes and McCulloch (2001)	1) Large collagen fibres in MI scar are considered. 2) Guccione McCulloch and Waldman (1991) model is updated to include transmurally variable collagen fibres. 3) Five model constants are decided by directional vector components measured from the mean collagen fibre angle and weighted histological collagen fibre area fractions.	[81]
LV aneurysm models	Rigid model	Vayo (1966)	1) LV aneurysm is rigid or un-deformable. 2) LV is a spherical membrane. 3) LV chamber volumes are modelled at ED and ES.	[87]
	Deformable multilayer model	Lowe and Love (1948)	1) LV and aneurysm are in three-layer structure and keep spherical in cardiac cycle. 2) MI layers are in liquid state 3) Each layer thickness in MI is equal to that in remote region. 4) Centres of two spherical surfaces of inner and outer segments remain fixed. 5) Two stress ratios are related to muscle length linearly. 6) Isometric contraction phase is modelled.	[88]
		Radhakrishnan, Ghista and Jayaraman (1980)	3) Each layer volumes remain unchanged. 4) Centres of two spherical surfaces of inner and outer segments are different. 1), 2), 5) and 6) are the same as the Lowe and Love (1948) model above.	[92]
		Radhakrishnan, Ghista and Jayaraman (1986)	6) LV is in ellipsoidal shape and aneurysm is spherical in cardiac cycle. 1) to 5) are the same as the Lowe and Love (1948) model above.	[93]
	Deformable multilayer model with nonlinear myocardium	Mirsky, McGill and Janz (1978)	5) Two stress ratios are related to muscle length nonlinearly. 6) Diastole is modelled. 1) to 4) are the same as the Lowe and Love (1948) model above.	[94]
	Single-layer balloon with nonlinear myocardium	Bogen and McMahon (1979)	1) LV is a spherical single-layer balloon initially but deformed into an axis-symmetrical structure in diastole. 2) Strain energy function of rubber-like mater is adopted for myocardium and aneurysm but with different material constants. 3) Diastole is modelled.	[97]
	Stress-strain model	Parmley, Chuck, Kivowitz, et al (1973)	Uniaxial stress-strain data of human fibrous, fibrous and muscular and muscular aneurysms are fitted by exponential function	[99]
	Strain energy function for isotropic aneurysms	Janz and Walderon (1978)	1) Strain energy function is composed of three principal stretches with a power constant and Poisson ratio without invariants. 2) Two model constants are determined by fitting diastolic *p*-*V* curves.	[100]
	Exponential strain energy function for anisotropic aneurysms	Guccione, Moonly, Moustakidis, et al (2001)	1) Fung type strain energy function is used. 2) Four model parameters for passive state are decided at ED. 3) One model constant is determined at end-isometric contraction.	[50,56]

Table 1 Summary of biomechanical models for LV growth and remodelling after MI (continued)

Classification		Contributor	Feature	Ref
Growth models	Collagen concentration model	Jin, Han, Berger, et al (2011)	1) Macrophage, fibroblast, TGF-β, MMM-p and collagen I are key factors regulating collagen fibre growth and degradation. 2) Pathways for collagen fibre growth and degradation are clarified. 3) ODEs of concentration change rate of these factors are established. 4) ODEs are solved and intervention effect on collagen concentration is identified.	[120]
	Agent-based fibroblast growth model	Rouillard and Holmes (2012)	1) Chemokine in MI scar drives fibroblast growth and death. 2) Fibroblasts control collagen fibre growth/degradation and orientation under various cue conditions. 3) Non-collagen fibres are with degradation only. 4) Fibroblasts are assumed to be discrete discs, and the rest variables are continuous.	[122]
	Coupled 2D agent-based model and FE model	Rouillard and Holmes (2014)	1) Fibroblast production/destruction and orientation are modelled with agent model under chemical and mechanical cues. 2) Collagen fibre growth/degradation and orientation depend on fibroblasts. 3) FE model and growth model are coupled to provide mechanical cue. 4) 2D planar scar is modelled at ED.	[125]
	Coupled 3D agent-based model and FE model	Zhuan, Luo, Gao, et al (2019)	1) LV wall is full of collagen fibre which is in myofibre direction. 2) Fibroblast production/destruction and orientation are modelled with agent model under chemical and mechanical cues. 3) Collagen fibre growth/degradation and orientation depends on fibroblasts. 4) FE model and growth model are coupled to provide mechanical cue. 5) Idealized rat LV are modelled at ED.	[126]
	Growth in one direction	Klepach, Lee, Wenk, et al (2012)	1) Myofibre rather than collagen fibre growth along myofiber is modelled. 2) Myofibre orientation remains unchanged. 3) Growth doesn't affect sheet direction but results in shrinkage in cross-fibre direction. 4) Growth is driven by steady increasing cyclic Cauchy stress. 5) Realistic LV and ED arer modelled.	[127]
	Growth in two directions	Saez and Kuhl (2016)	1) Collagen fibre growth and myocyte death are considered in terms of short supply in oxygen. 2) Growth/degradation is along myofiber and sheet directions. 3) Realistic LV and ED are modelled.	[128]
	Integrated electro-mechanical-growth	Lee, Sundnes, Genet M, et al (2016)	1) Electrophysiological, biomechanical, and tissue growth models are integrated. 2) Growth occurs in mayordom of remote and border only. 3) Collagen fibres in MI are without growth and orientation change. 4) Realistic LV and *p-V* loop are modelled.	[129]

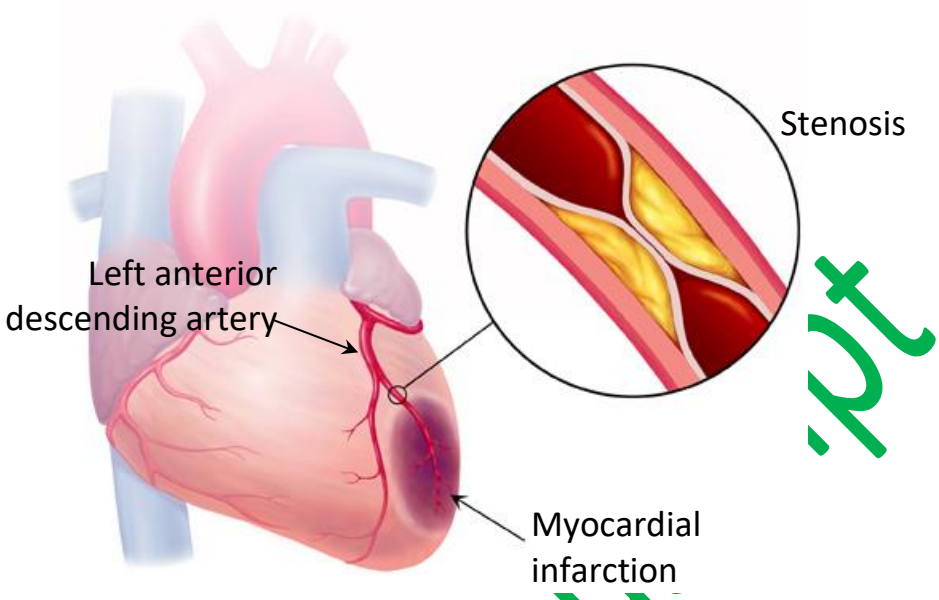

Fig. 1 Myocardial infarction caused from stenosis in left anterior descending (LAD) coronary artery, the picture is from ttps://www.theexpertinstitute.com/case-studies/cardiologist-misses-mi-resulting-in-fatal-arrhythmia/

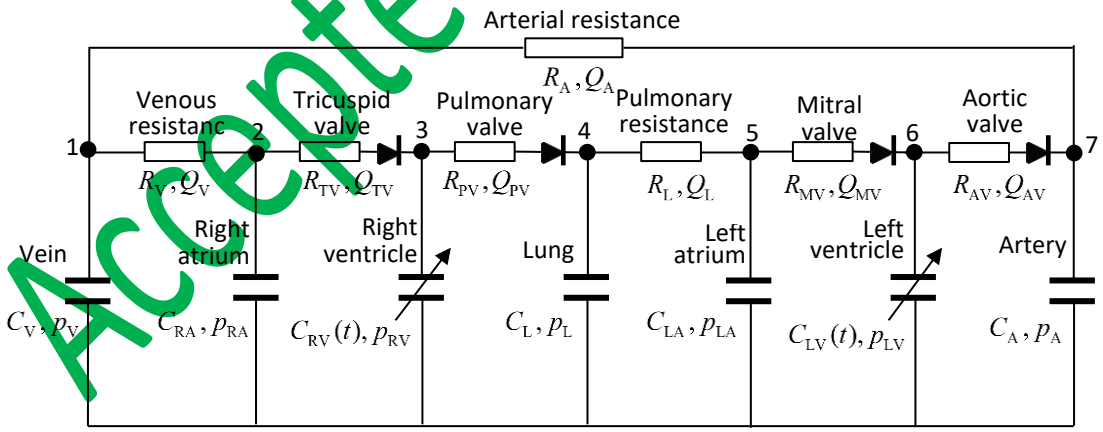

Fig. 2 A lumped-parameter cardiovascular blood flow model, at note 1 to 7, the Windkessel model and flow rate balance equation are applied, four valves are simplified to a series resistor and unidirectional diode, respectively.

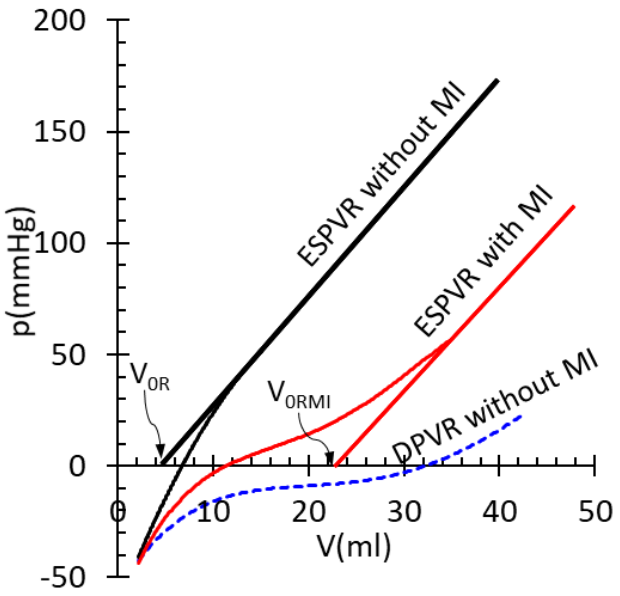

Fig. 3 End-systolic pressure-volume relations (ESPVR) measured in vitro from a dog LV, MI was created by ligating left circumflex arteries in the LV, the plot is adapted from [32].

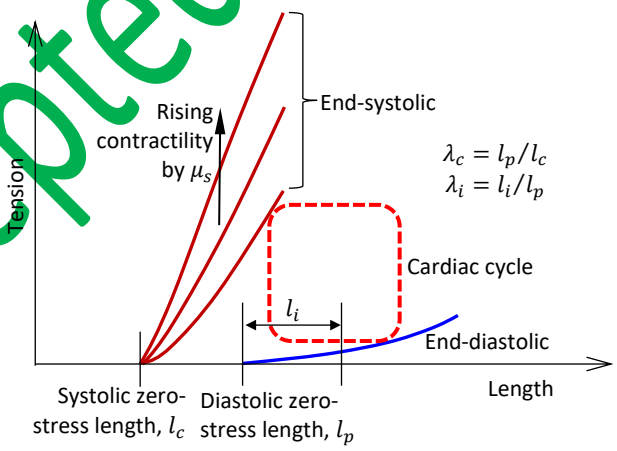

Fig. 4 Myocardial end-systolic and diastolic tension-length curves, λ_c is defined by systolic rest length l_c, and diastolic rest length l_p, λ_p is done by instant diastolic length l_i and l_p, alternating μ_s can change ESPVRs.

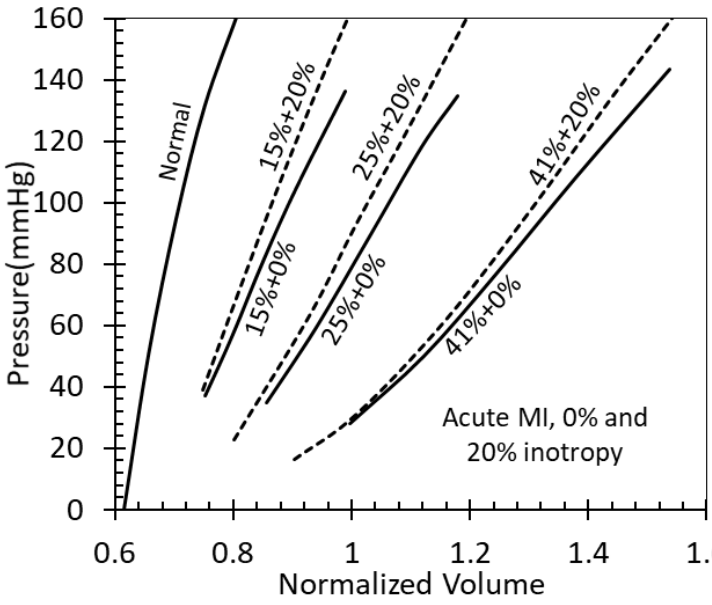

Fig. 5 ESPVRs predicted based on constitutive laws and input data by using FEA of axis-symmetrical membrane LV model in [41], MI sizes are 15%, 25% and 41%, respectively.

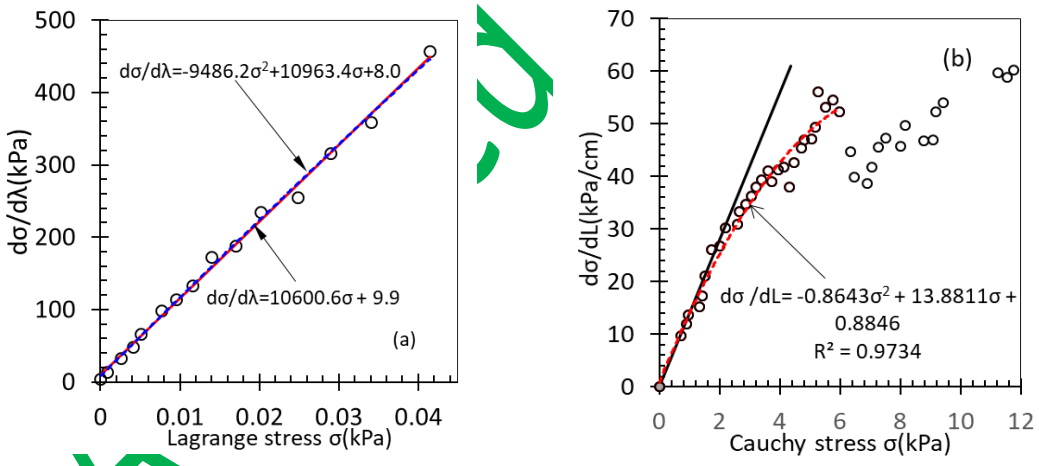

Fig. 6 Experimental data and fitted curves for stress-stretch or length curve slope $d\sigma/d\lambda$, $d\sigma/dL$ in terms of stress σ (a) ribbit mesentery, (b) ribbit LV wall at 2d after MI

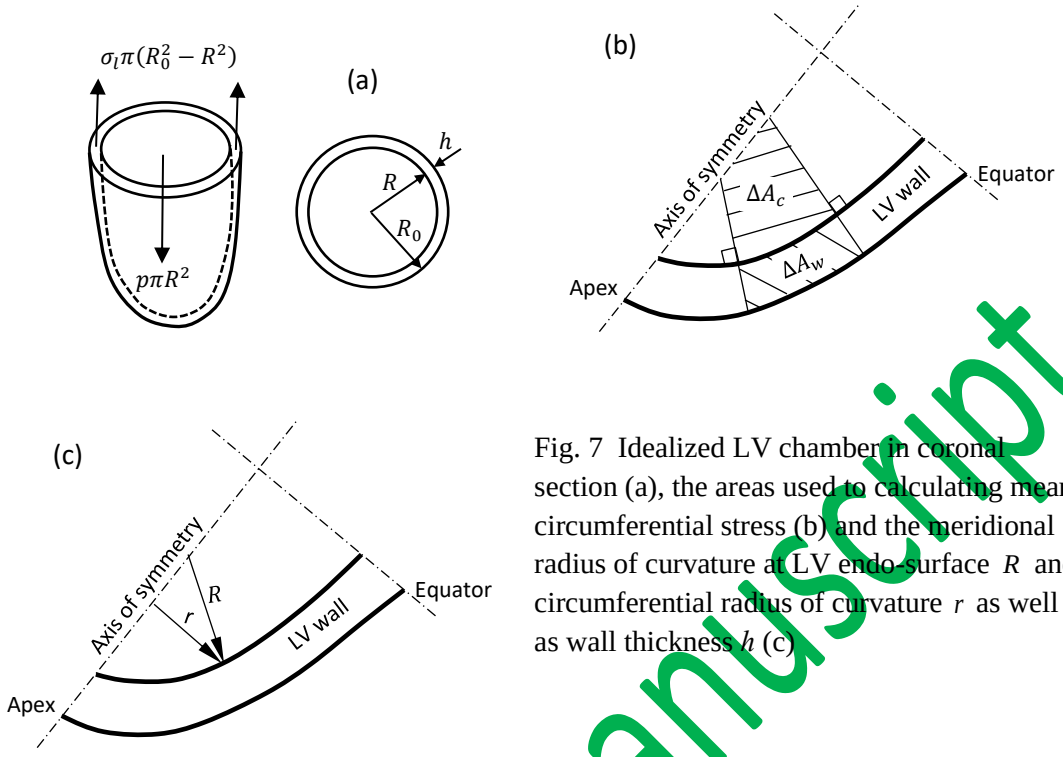

Fig. 7 Idealized LV chamber in coronal section (a), the areas used to calculating mean circumferential stress (b) and the meridional radius of curvature at LV endo-surface R and circumferential radius of curvature r as well as wall thickness h (c)

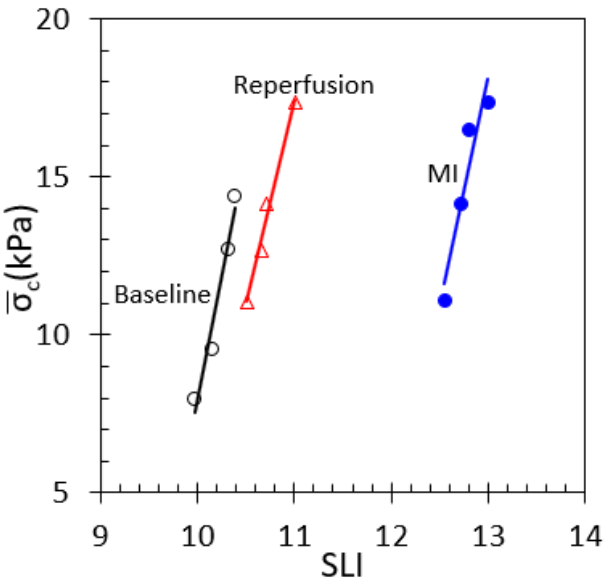

Fig. 8 The relation between the systolic length index (SLI) and end-systolic regional wall stress $\overline{\sigma}_c$

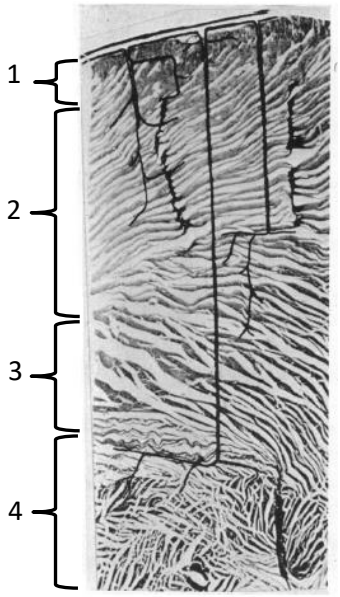

Fig. 9 Layer structure of LV wall, the picture is from [89], 1-pericardial superficial sino-spiral muscle, 2-deep sino-spiral muscle, 3-deep bulbo-spiral muscle, 4-endocardial superficial bulbo-spiral muscle

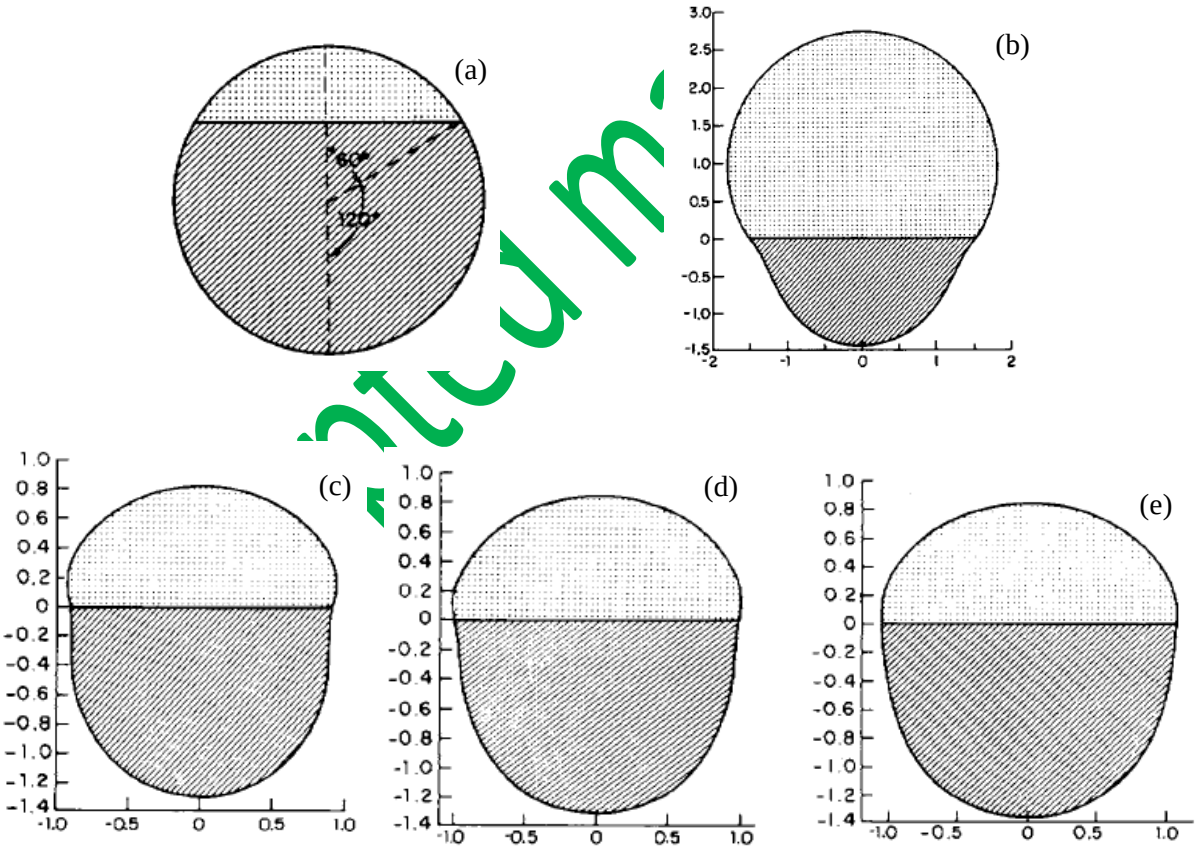

Fig. 10 LV initial spherical shape with an infarcted zone on top of 60° damage angle (a), and predicted blowout aneurysm with k =2 in diastole (b), three aneurysms predicted during systole at ESPs of 50, 100 and 150mmHg, respectively, (c)-(e), the pictures from [97]

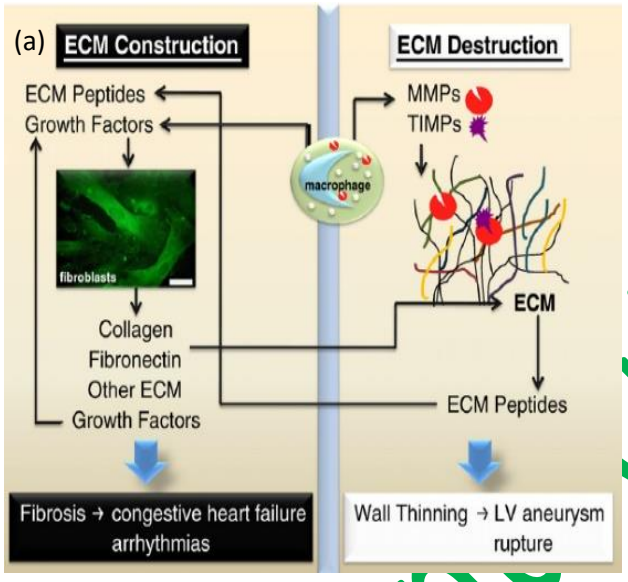

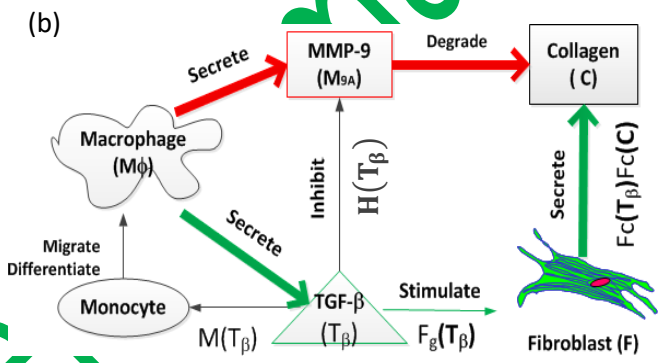

Fig. 11 Macrophage regulates ECM construction and destruction (a) and pathways of macrophage regulating collagen construction and destruction (b), (a) is from [119], (b) is after [120]